Towards a Coupled Multi-Scale, Multi-Physics Simulation Framework for Aluminium Electrolysis

Kristian Etienne Einarsrud[1*], Ingo Eick[2], Wei Bai[3], Yuqing Feng[4], Jinsong Hua[5], Peter J. Witt[4]

[1] Department of Chemistry and Material Science, Faculty of Technology, Norwegian University of Science and Technology (NTNU), 7030 Trondheim, Norway

[2] Hydro Aluminium, Koblenzerstrasse 122, 41468 Neuss, Germany

[3]SINTEF Materials and Chemistry, 7465 Trondheim, Norway

[4] CSIRO Mineral Resources, Bayview Avenue, Clayton, VIC 3168, Australia

[5] Institute for Energy Technology (IFE), 2027 Kjeller, Norway

[*]Corresponding author, E-mail address: kristian.e.einarsrud@ntnu.no

Abstract

Aluminium metal production through electrolytic reduction of alumina in a cryolite bath is a complex, multi-physics, multi-scale process, including magneto-hydrodynamics (MHD), bubble flow, thermal convection, melting and solidification phenomena based on a set of chemical reactions.

Through interactions of the different forces applied to the liquid bath combined with the different time and length scales, self-organised fluctuations occur. Moreover, the MHD behaviour causes a complex metal pad profile and a series of surface waves due to the meta-stable condition of the metal / cryolite interface.

The large aspect ratio of an industrial cell, with a footprint of 20 by 4 m and at the same time having dimensions approaching just 30 mm of height for the reaction zone, prevents an integrated approach where all relevant physics are included in a single mathematical model of this large degree of freedom system. In order to overcome these challenges, different modelling approaches have been established in ANSYS FLUENT; Three models are used to predict details of specific physics: one to predict the electro-magnetic forces and hence the metal pad profile, a second that resolves details of the local bubble dynamics around a single anode and a third for the full cell bath flow. Results from these models are coupled to allow integration of the different phenomena into a full cell alumina distribution model. The current paper outlines each of the approaches and presents how the coupling between them can be realized in a complete framework, aiming to provide new insight into the process.

Highlights

- Scales of the process in length and time are identified for aluminium electrolysis.
- Four modelling approaches describing essential features are presented.
- Coupling between modelling approaches is discussed and demonstrated.

Keywords

Aluminium Electrolysis, Computational Fluid Dynamics, MHD, Multi-Scale Modelling

1 Introduction

Electrolytic aluminium metal production is a multi-scale, multi-physics process with a high degree of coupling between the pertaining non-linear forces. These coupling conditions result in a complex system, which can introduce collective behaviour, resulting in a self-organized pattern [4].

To better understand the self-organized pattern and the overall process, modelling of the main dynamic contributors, which are the magnetic field forces and the bubble draft forces, is the most sensible approach, as the harsh, hot and corrosive industrial operating conditions prevent access for easy visual inspection and measurement.

The main forces are driven by an imposed external electrical current, the main purpose of which is driving the chemical reduction reactions. These reactions cause changes in the species concentrations and distributions that affect the bulk and surface properties, all of which influence the various forces and reactions.

The current paper aims to describe how a modelling approach can be designed to generate insight and support potline operation.

After sketching the main process phenomena of the aluminium electrolysis process, different modelling approaches are described; three of which predict details of specific physics: the electro-magnetic forces and hence the metal pad profile, details of the local bubble dynamics around a single anode and the full cell bath flow. Coupling between two of the approaches is then demonstrated in a fourth model, aiming to describe the distribution of alumina in a full cell geometry. Finally, further coupling is discussed aiming towards a framework which can generate new insight on cell performance.

2 Main Process Phenomena

The primary process phenomena are triggered by an electrical current conducted through the production system. The current drives the electrolysis reactions that generate gas bubbles, set into motion by buoyancy. The buoyant bubbles and the establishment of an induced magnetic field from the current result in Lorentz forces that are the main driving forces for the bath and metal flows, respectively.

2.1 Magnetic fields

In modern aluminium smelters, 150 – 450 electrolysis cells are connected side by side in a row up to 1.7 km long; the exact number depends on the rectiformer capacity which ranges between 800 – 2000V. At each cell a voltage drop of between 4 and 4.5 volts occurs consisting of alumina dissociation (1.7V), various over-voltages (0.4V), solid conductors (0.6V), as well as about 1.5V for maintaining the inner heat. This huge current loop is operated with current load in the range of 150000 to 600000 Ampere and built up out of a busbar system of large aluminium slabs. This system, which for geometrical reasons is separated into 1-3 potrooms, generates magnetic fields with magnitude typically of order 100 Gauss, depending on design and current load. The 15-20 mm thick steel shell of each cell will reduce and modify the magnetic field before it generates Lorentz forces on the moving liquid metal and cryolite bath inside the electrolysis cell [17].

With the increased current load of the recent decades, longer and longer shells of up to 30 m in length with a common width of about 4 m have been developed. So finally, the length scales from the steel shell thickness up to potroom dimensions define the active magnetic field, which is established in milliseconds.

2.2 Bubble flow

The electrical current is distributed to 20 to 48 parallel-connected anodes in the cell, resulting in a typical anodic current density of 0.8 to 1.0 A/cm^2. Based on Faraday's law, the applied current controls the rate of reaction ($2Al_2O_3 + 3C \Rightarrow 3CO_2 + 4Al$) for the dissolved alumina at the carbon anode that generates CO_2 gas bubbles. It is not fully understood whether these bubbles are nucleating out of an oversaturated cryolite bath at the anode bottom, or by a competing process that is absorbing dissolved CO_2 in the anode structure that gives rise to bubbles at the surface but, ultimately, bubbles will be generated on the anode surface. The bubbles, which accumulate under the anode by coalescence, will move with the passing bath or due to anode shape and rise around the anode. These rising bubbles displace bath at the ends and sides of the anodes that results in bath circulation within the channels and leads to large scale circulation within the entire cell [7]. This meso-scale process,

starting with about 0.4 mm small nucleated bubbles, finally results in large rising plugs of gas with a length scale of 10-20 cm with self-organising fluctuations having frequencies of 0.2 – 2 Hz.

2.3 Bath and metal flow

Inside the electrolysis cell, liquid metal and cryolite bath, operating at about 950°C, are separated into two layers, about 200 mm thick, by the relatively small density difference (metal 2270 g/cm^3, bath 2070 g/cm^3) and surface tension of about 0.56 N/m. In the macro-scale flow domain of the full cell, the magnetic field shapes the circulating metal layer by Lorentz forces [26], which further induces local currents and fields. Besides the magnetohydrodynamic (MHD) stirring of the metal pad, the gas bubbles cause stirring of the bath layer. Here the shapes of the anode and side ledge profiles are significant in affecting the established flow pattern.

Compared to the shell length, the narrow reaction zone is only 30-40 mm between the anode bottom and the wavy upper interface of the metal, called the anode cathode distance (ACD), so a large range of length scales are defining the bath flow. The typical flow speed is between 10 and 20 cm/s resulting in a circulation time of 100 seconds along the cell and about 10 seconds along a typical 1500 mm long anode.

2.4 Reactions

Alumina particles are fed to the cell at several locations, with about 0.2-1 kg per shot once a minute depending on the required consumption. Superimposed on to the average consumption is the so-called demand feeding regime where the feed amount is varied in a 2-3 hour cycle by about ± 10-20% for process control reasons. The chemical process can be split into four main reactions based on six species (Al_2O_3, $Na_2Al_2O_2F_4$, $Na_2Al_2OF_6$, Na^+, NaF, AlF_3) covering the dissolution of alumina particles to the accumulation of aluminium metal at the cathode.

- **Dissolution** of alumina particles into the bath through the reaction:

$$2\ Al_2O_{3(s)} + 6\ NaF + 2AlF_3 \overset{k1}{\rightleftharpoons} 3\ Na_2Al_2O_2F_4 \quad (1)$$

- **Equilibrium** bath reaction:

$$3\ Na_2Al_2O_2F_4 + 6\ NaF + 6\ AlF_3 \overset{k2}{\Leftrightarrow} 6\ Na_2Al_2OF_6 \quad (2)$$

- **Anode** boundary layer reaction:

$$6\ Na_2Al_2OF_6 + 3\ C \overset{k3}{\rightleftharpoons} 12e^- + 12\ AlF_3 + 12\ Na^+ + 3\ CO_2 \quad (3)$$

- **Cathode** or metal pad boundary layer reaction:

$$4\ AlF_3 + 12\ Na^+ + 12e^- \overset{k4}{\rightleftharpoons} 4\ Al + 12\ NaF \quad (4)$$

The dissolution process can take several minutes depending on factors such as feeding shot size, feed dispersion, agglomeration, local species concentration, temperature and flow speed in the bath [36]. Species concentrations affect bulk properties of the bath including density, viscosity and electrical conductivity, which further influence the local anodic current and the bath flow. Additionally the species change bubble-surface conditions through surface tension and contact angles, which are coupled to the bubble flow [32].

2.5 Performance

Cell performance is strongly reliant on a stable alumina concentration in the reaction zone below the anode. Shortage of alumina results in a parasitic reaction, with back reaction of the metal and generation of additional emissions. Properly selected feeder positions and variable local feeding doses ensure stable cell operation and high efficiency [22]. Consequently, the ability to realistically describe the alumina distribution in the cell is of high relevance to the industry.

3 Model Description

3.1 Metal pad profile model

The metal pad profile model aims to describe the steady state shape of the bath-metal interface under the action of gravity and MHD forces, by marching a transient simulation towards statistically steady state conditions. The motivation for a separate metal pad profile model is to provide relevant boundary conditions to models which focus on gas-bath flow.

3.1.1 Equations for fluid flow

The Volume of Fluid (VOF) method in ANSYS Fluent is used to simulate the dynamics of the bath-metal immiscible fluid system. A single set of momentum and continuity equations are solved to track the transient distribution of each fluid volume fraction within the computational domain, as described in Hua *et al.* [17]. The governing equations of the continuity and momentum conservation for the two-phase flow system with incompressible fluids are expressed as:

$$\nabla \cdot \mathbf{u} = 0 \tag{5}$$

$$\frac{\partial}{\partial t}(\rho \mathbf{u}) + \nabla \cdot (\rho \mathbf{u}\mathbf{u}) = -\nabla P + \nabla \cdot \left[\mu\left(\nabla \mathbf{u} + \nabla \mathbf{u}^T\right)\right] + \mathbf{F}_E + \rho\, \mathbf{g} \tag{6}$$

where $\mathbf{u}$ represents the flow field, P is the pressure, and $\mathbf{g}$ refers to the gravitational acceleration. $\mathbf{F}_E$ represents the volumetric density of external body forces such as the electromagnetic force, also

known as the Lorentz force. ρ and μ are the fluid density and viscosity, respectively. For this two-fluid system, the fluid properties (ρ and μ) are calculated with fluid volume fraction weighted averaging:

$$\rho = \rho_1 \alpha_1 + \rho_2 \alpha_2 \tag{7}$$

$$\mu = \mu_1 \alpha_1 + \mu_2 \alpha_2 \tag{8}$$

where the subscripts 1 and 2 denote the primary phase and the secondary phase, respectively, and α is the fluid volume fraction. The bath layer is set as the primary phase, and the metal layer as the secondary phase.

The distribution of the volume fraction for each phase and the tracking of the phase-interface is accomplished by solving the continuity equation for the volume fraction of the secondary phase (α_2):

$$\frac{\partial \alpha_2}{\partial t} + \mathbf{u} \cdot \nabla \alpha_2 = 0 \tag{9}$$

The primary-phase volume fraction (α_1) will be determined by the phase continuity constraint: $\alpha_1 = 1 - \alpha_2$.

3.1.2 Equations for electrical field and Lorentz force field

The Lorentz force ($\mathbf{F}_E$) is needed to close the governing equations for fluid flow. The electric current density $\mathbf{J}$ is calculated from Ohm's law taking into account the induced currents caused by the moving conductive liquid with velocity $\mathbf{u}$ in an external magnetic field $\mathbf{B}$:

$$\mathbf{J} = -\sigma \nabla \varphi + \sigma (\mathbf{u} \times \mathbf{B}). \tag{10}$$

Current conservation implies that the electrical potential φ can be obtained by solving the potential equation

$$\nabla \cdot (\sigma \nabla \varphi) = \nabla \cdot (\sigma \mathbf{u} \times \mathbf{B}). \tag{11}$$

For simplicity, the induced magnetic field due to the electric current flowing through the analyzed aluminum reduction cell is neglected in the current numerical model.

A volume fraction weighted harmonic average method is needed to correctly calculate the distribution of electrical conductivity over the metal-bath interface, and conserve the electric current in the numerical discretization of (11):

$$\frac{1}{\sigma} = \frac{\alpha_1}{\sigma_1} + \frac{\alpha_2}{\sigma_2}. \tag{12}$$

Finally, the Lorentz force density is given as

$$\mathbf{F}_E = \mathbf{J} \times \mathbf{B}, \tag{13}$$

where **B** is a *predefined* magnetic field mimicking that expected in a conventional aluminium reduction cell. The calculated Lorentz force is included in the source term ($\mathbf{F}_E$) of the momentum equation (6).

3.1.3 Turbulence

To limit the complexity of the problem, the standard k-ε turbulence model with standard wall functions is used to calculate the turbulent viscosity in the each phase. Our numerical exercises [17] indicate that the standard k-ε turbulence model could make reasonable predictions with relatively coarse meshes, which will shorten the total calculation time required for the transient simulation of the metal pad profile development in the aluminum electrolysis cells. The deficiencies of the k-ε turbulence model for such type of flows, where recirculation and re-attachment could occur at the boundary layer, are well known (cf. Pope [24]) and alternative turbulence models could be a better choice, but ultimately require an exceedingly fine meshing for the boundary layer and long calculation time for the current application.

3.1.4 Model configuration

3.1.4.1 Geometry

A rectangular box model, which has the dimensions close to those of the industrial scale electrolysis cells, is shown in Figure 1. The aluminium electrolysis model has 20 anodes, length of 12 m and width of 4 m. The mean height of the metal layer is 0.2 m, and the bath layer height is 0.18 m. The distance between anode and metal-bath interface (ACD) is set to be 0.045 m. The width of central and side channels is 0.15 m, and the width of cross channels between the anodes is 0.05 m. It should be noticed that the cell geometry details allowed to publish here is based on a benchmark model and it is different from the actual cell geometry used for bath flow model in Section 3.3.2

The computational mesh used for the CFD analysis is shown in Figure 2. In general hexahedral cells are used. In the horizontal directions, the central channel and cross channel are meshed with four cells, the side channel is meshed with six cells and each anode is meshed with 20×12 cells. In the vertical direction, the model is divided into three zones. The top zone covers the channel height (bath

layer above ACD region), is 0.135 m in height and is meshed with 8 cells. The middle zone is the interface deformation zone, with a relatively fine mesh. It has a thickness of 0.125m that covers the ACD region and part of the metal layer, and is meshed with 10 cells. The bottom zone, which has a height of 0.12 m, is meshed with 6 cells. The CFD model contains 187,392 hexahedral cells.

It should be noted that the effect of side ledge profile can also be taken into account in generic realistic models for aluminum reduction cells. However, results in this section focuses on the simplified rectangle box model, neglecting slanted side ledge profile.

3.1.4.2 Properties

In the CFD model setup, the material properties for the fluids, electrolyte and liquid aluminum are required; they are summarized in Table 1.

3.1.4.3 Boundary conditions

For fluid flow, no slip boundary conditions are applied on all wall surfaces. The free surface on top of the bath is treated by applying no slip boundary conditions and surface effects such as waves are ignored. Standard wall functions are assumed on all solid walls for the k-ε turbulence model.

As for the boundary conditions of the electric potential equation, zero electric potential is set on the bottom and side of anode, while electrical insulation conditions are applied on the side walls, where the current density is set to zero. Since the fluid velocity on the side walls is assumed to be zero, the zero-flux condition is used for the electrical potential calculation. The assumed normal current density (A/m^2) on the cathode surface is specified explicitly by the normalized length $\upsilon=y/y_o$ along the cathode block as:

$$J_z = J_o \cdot (-2181 - 3013\upsilon^2) \tag{14}$$

with J_o as nominal current density. The proposed current density, centered in the centre channel, simulates the main characteristics of an aluminium reduction cell i.e. increasing current pick-up along the cathode block, corresponding in shape to that proposed by Severo *et al.* [27].

The magnetic field consists of the field generated from the external current carrying parts such as bus bars, and the field generated from the current flowing inside the cell. In order to calculate the magnetic field generated from the external current carrying parts, the model should also include the configurations of pot lines and bus bars, as well as a thermo-electrical model, which is beyond the simulation framework reported in this paper. The induced magnetic field could in principle be calculated in the current approach, although at the cost of a further increase in calculation time, only

yielding a minor contribution to metal pad heaving and metal speed. For simplicity, the following (steady) magnetic field (mT) is imposed on both bath and metal layers:

$$\begin{cases} B_x = B_o \cdot (-1.5 - 0.2\xi + 8.0\upsilon - 0.05\xi\upsilon) \\ B_y = B_o \cdot (-0.7 - 1.0\xi + 0.2\upsilon - 0.01\xi\upsilon) \\ B_z = B_o \cdot (-0.02 - 0.1\xi - 0.5\upsilon - 0.7\xi\upsilon) \end{cases} \quad (15)$$

based on the normalized dimensions $\xi=x/x_o$ and $\upsilon=y/y_o$ with x_o and y_o according to unit length and B_o nominal magnetic field. This is a best fitted correlation obtained from results of an in-house magnetic field model for practical reduction cells and shows the main characteristics of those in operating aluminium reduction cells.

As in previous benchmarks (Severo *et al.,* [27]), the Ampere-Maxwell equation

$$\nabla \times \mathbf{B} = \mu_0 \mathbf{J} \quad (16)$$

is not fulfilled for the artificial magnetic field and the chosen current boundary condition for electrical current density, owing to the qualitative nature of the proposed fields in eqn (15). The significance of the above inconsistency is currently not known. However, based on the relatively good match between simulations and experiments (cf. Severo *et al.*, [27] and the current work), it is expected that the importance of inconsistency is of lower order. A possible explanation is that equation (16) is not explicitly utilized in the proposed model [17].

Aluminium electrolysis at the anode surface causes consumption of the carbon anode material, and as described by eqn (3), the rate of consumption is a function of the local current density. Areas of the anode that have a high current flow will be more rapidly consumed, thus increasing the ACD at that point, which will then increase the voltage drop over the ACD and subsequently lower the current at that point. This behavior tends to a stable state with a uniform voltage drop over the ACD and a near uniform current density, consumption rate and ACD such that the profile of the anode base tends to match the shape of the metal pad. To account for the consumption of anode material, a constant ACD condition is applied in the model. Hence, the anode is adjusted according to the shape of metal pad. To achieve this in the current model, the ANSYS Fluent dynamics mesh model and sliding mesh interface is activated, and a set of UDF functions is programed to move the anode bottom mesh accordingly.

3.1.4.4 Initial conditions

The initial fluid velocity inside the reduction cell is assumed to be zero. The electric potential is also set to zero. The metal/bath interface is initialized as a flat horizontal surface with a height of 0.2 m. The bath layer rests above the liquid metal layer.

3.1.4.5 Simulation schemes

The following numerical schemes provided by ANSYS Fluent were applied: "SIMPLE" for pressure-velocity coupling, the spatial discretization scheme "PRESTO!" for pressure, the "Geo-Reconstruct" scheme for volume fraction, and "First Order Upwind" for other equations.

A transient simulation is adopted in the modeling using the "First Order Implicit" scheme with a constant time step of 0.04s.

In ANSYS Fluent, various numerical approaches are implemented for solving the secondary phase volume fraction, equation (9). The geometric reconstruction scheme is used for interface tracking in the current approach to maintain the interface sharpness.

3.2 Transient mesoscale bubble model

A mesoscale model has been developed, aiming to describe details of the bubble behaviour on the scale of a single anode, considering gas and bath flow. The ultimate goal is to develop a numerical "laboratory" from which relevant closure relations, such as drag laws, can be obtained and used in large scale models that describe global features of the full cell. Such a mesoscale model could also be used to probe details of bubble formation and evolution. The principal features of the proposed modelling framework is given in the following, while further details can be found in Einarsrud [5] and Einarsrud et al. [6], [7] and [8].

The model is a multiscale and multi-field approach, aiming to fully resolve the behaviour of macroscopic anodic bubbles (down to a few millimetres), while phenomena occurring at smaller scales (for instance nucleation of small bubbles) is treated by means of applicable sub-grid models. The proposed modelling framework consists of five fields, as shown in Figure 3.

Considering CO_2 as an example, it is produced on the anode surface owing to the presence of an electrical current, resulting in a field of dissolved CO_2, i.e. gas is on a molecular level assumed to saturate the molten bath in proximity of the anode. As concentrations approach saturation, gas bubbles nucleate and form a dispersed bubble field, which evolves by means of coalescence and mass transfer, treated by means of a discrete population balance model (PBM) in the current

formulation. Upon reaching a critical volume fraction, the dispersed bubble field is converted to a continuous (fully resolved) field, treated by means of the Volume of Fluid (VOF) approach.

The outer fields depicted in Figure 3 are transported and coupled to the flow fields, while the behaviour of the electromagnetic fields (i.e. current density) and flow fields are coupled to the various material properties (e.g. electrical conductivity and viscosity) determined by the relative concentrations of dissolved species and dispersed and continuous gas fields. Evidently, the proposed modelling framework is capable of dynamically predicting, for instance, anodic voltage oscillations, which arise due to the quasi-periodic formation and release of anodic gas bubbles.

3.2.1 Electromagnetic fields

The electrochemical reactions occurring in the cell are driven by an external electrical current, i.e. the principal reactions are considered to be governed by Faraday's law. The electrical current density **J** is given in equation (10) without the second summand for induction currents, which are neglected as these typically are small in the bath. The electrical potential is determined by the Poisson equation (equation 11) resulting from the requirement of current conservation. The electrical conductivity depends upon local specie and gas concentrations and the electrical current density will thus vary both spatially and temporally, depending for instance upon gas coverage.

The electrical current density also promotes a momentum source though the Lorentz force, defined as in equation (13).

3.2.2 Dissolved fields

Seven separate species are considered; Al_2O_3, NaF, AlF_3, $Na_2Al_2O_2F_4$, $Na_2Al_2OF_6$, Na^+ and CO_2. The first six correspond to those proposed by Witt et al. [36] aiming to represent the principal components of the bath, while CO_2 is modelled as a dissolved specie in the bath. All species (Y_i) are treated by a generic advection-diffusion equation

$$\frac{\partial \rho_b Y_i}{\partial t} + \nabla \cdot (\mathbf{u}\rho Y_i - \rho_b D_i^e \nabla Y_i) = S_i^p - S_i^c \tag{17}$$

on a mass fraction basis, where D_i^e is the effective diffusivity (including turbulent diffusion $D_i^t = \nu_t / 0.9$, ν_t being the turbulent viscosity, where applicable) and S_i^p and S_i^c respectively represent source and sink terms due to production and consumption of the *i*-th specie, for instance due to electrochemical reactions and nucleation for CO_2. Relevant reaction schemes are described in section

2.4 and details regarding the form of the source terms can be found in Witt et al. [36] and Einarsrud *et al.* [8].

3.2.3 Dispersed fields

The dispersed field is concerned with small scale bubbles, typically ranging from a diameter of 0.4 mm (observed nuclei) and up to sizes dictated by the numerical resolution, typically 1-3 mm. The sub grid bubbles are treated by means of a discrete population balance model (PBM), with the following conservation law for the number density of the *i*-th bubble size, $n_i(x,y,z,t)$;

$$\frac{\partial n_i}{\partial t} + \nabla \cdot (\mathbf{u} n_i - D_{PBM} \nabla n_i) = b_i - d_i \tag{18}$$

where n_i is the number density, D_{PBM} is a diffusion coefficient and b_i and d_i respectively represent birth- and death rates for the given bubble class. Birth- and death rates involve phenomena related to nucleation (for the smallest bubbles), coalescence and mass transfer, details of which can be found in [6].

Dispersed bubbles are modelled by means of a discrete population balance model with an exponential discretization, $V_{i+1} = qV_i$, i.e. the average bubble volume in a given bin *i+1* is proportional to that of the neighbouring bin *i*.

As the dispersed bubbles grow in size they eventually reach a size corresponding to the numerical resolution at which stage they are transferred to the continuous field, through an intermediate bubble class, as described in [5] and [6].

3.2.4 Continuous and flow fields

The continuous (resolved) fields are treated by means of the Volume of Fluid (VOF) method, allowing for direct simulations of the complex bubble topology present on the anode surface. In the VOF-method, the evolution of the *k*-th continuous field with density ρ_k is governed by a phase fraction equation of the form

$$\frac{\partial \alpha_k \rho_k}{\partial t} + \nabla \cdot (\alpha_k \rho_k \mathbf{u}) = S_k^{\alpha} \tag{19}$$

where S_k^{α} is a source term originating from interactions with sub-grid entities, i.e. production of macroscopic gas bubbles from the dispersed elements and coalescence between large resolved

bubbles and dispersed bubbles. A single flow field is shared between the phases, governed by the incompressible Navier-Stokes equations, i.e. equation (6), with additional terms relating to surface tension as of the continuum surface stress model, cf. Laufaurie *et al.* [19], Lorentz-forces as of equation (13) and turbulence enhanced viscosity, as of the realizable $k-\varepsilon$ -model (Shih *et al.* [28]). It should be noted that the current formulation implies that turbulence is shared between the phases, i.e. no special attention is given to the transfer of turbulent properties on gas-liquid interfaces. Owing to the close resemblance between simulations and experiments (cf. [8] and [29]), such phenomena are however expected to have small impact on the overall anodic bubble behaviour.

3.2.5 Properties

In the current formulation, large scale properties, i.e. density and viscosity are dependent upon the distribution of continuous fields, using the volume fraction of resolved gas and bath as a weighting function as of equations (7) and (8).

Microscopic properties, i.e. conductivity, surface tension and contact angles are dependent upon dissolved, dispersed and continuous fields, by means of applicable correlations such as for instance the Bruggeman correlation for conductivity. Details regarding relevant correlations can be found in [8].

3.2.6 Realization of mesoscale model

The model has been fully realized in ANSYS FLUENT R14.5, utilizing the user defined function and scalar functionality to extend the existing features to the current requirements. Details regarding the implementation can be found in Einarsrud [5] and [6].

3.2.7 Model configuration

3.2.7.1 Geometry, boundary- and initial conditions

A sketch of the 2D cross section of the domain studied in the mesoscale approach is given in Figure 4. Note that the metal pad is not treated explicitly in the mesoscale approach; instead adequate boundary conditions, e.g. relevant velocity and current density profiles, are given on the lower boundaries of the domain, obtained for instance from the metal pad profile model, or from specific experimental conditions as in [3]. The anode inclination, resulting from the requirement that the

anode remains parallel to the metal pad, is simulated by introducing a gravity vector with a given inclination compared to the z-direction. The upper boundary of the domain is treated as a single pressure outlet, while the remaining outer surfaces are treated as non-conducting, no-slip walls. The anode surface is considered as an equipotential surface with a distribution of active nucleation sites as described in [5].

The system is initialized at rest with gas and bath fully separated as indicated in Figure 4 and with species mass fractions corresponding to a total alumina content of 7.7 wt%, 7.8 wt% excess fluoride and an initial supersaturation of CO_2 of 3, as described in [8].

The geometry is meshed with quadrilateral cells, aiming at a resolution of 3 x 3 x 1 mm on the anode surface; the highest resolution being normal to the anode surface. The mesh is a compromise between the two approaches that constitute the mesoscale approach; on one hand, the mesh should be sufficiently coarse so that the sub-grid models actually are sub-grid, while on the other hand, the mesh should be sufficiently fine so that macroscopic (VOF) bubbles are (sufficiently) resolved. As shown in [5], doubling the proposed resolution influences the (principal) results by less than 10%, indicating that the proposed resolution is sufficient.

3.2.7.2 Simulation schemes

Simulations are performed using the pressure based solver where gradients are computed with a Green-Gauss cell based method and pressure velocity coupling is performed by the PISO algorithm with default correction factors for neighbour-skewness. The multiphase nature of the flow is treated by means of the explicit VOF model, discretized using the Geo-reconstruct scheme with surface tension activated. UDS equations are discretized using the QUICK scheme, while the remaining equations are discretized with the first order upwind method. The multigrid solver is set to a V-cycle for UDS equations for increased convergence rate, while the flexible cycle is used for pressure, for increased stability.

Time advancement is performed using the first order implicit scheme with a constant time step of 0.001 s. All other settings are kept at their default values.

3.3 Full cell bath flow model

Computational models of the electro-magnetic fields are widely used in industry to design cells. Only recently (Feng *et al.* [10], Witt *et al.* [35]) have detailed computational models of the molten liquid-gas bath become available. The CFD modelling approach used for the bath flow model is to solve a steady-state model for the bath and bubble flow within a cell. Then by holding the bath flow

fixed, a transient model of the alumina transport, feeding and consumption is used to predict the time varying alumina concentration in the cell.

Details of the CFD model physics, approach, mesh sensitivity, validation and implementation in ANSYS/Fluent have been previously documented in previous works (Feng *et al.* [10][11][12][13], Witt *et al.* [35]). For brevity only an overview of the bath flow model is presented here.

The bath flow model uses the Eulerian-Eulerian or two-fluid approach to solve time averaged transport equations for the gas and liquid phase velocities and volume fractions (*i=g,l*).

$$\nabla \cdot (\alpha_i \rho_i \mathbf{u}_i) = 0 \tag{20}$$

$$\nabla \cdot (\alpha_i \rho_i \mathbf{u}_i \mathbf{u}_i) = -\alpha_i \nabla P + \nabla \cdot (\alpha_i (\mu_i + \mu_{ti})(\nabla \mathbf{u}_i + (\nabla \mathbf{u}_i)^T) + \mathbf{S}_{Mi} + \mathbf{M}_i \tag{21}$$

Small-scale structures such as bubbles and turbulent structures are averaged in time and space necessitating the used of source terms $\boldsymbol{S}_{Mi}$, to account for buoyancy and the Lorentz force. Inter-phase terms, $\mathbf{M}_i$, are added for inter-phase drag, which is based on the Ishii and Zuber [18] model, and for the turbulent dispersion force based on the model of Lopez de Bertodano [20].

To account for turbulent effects the *k-ε* turbulence model with modifications for multiphase flow is solved for the liquid phase.

$$\nabla \cdot (\alpha_l \rho_l \mathbf{u}_l k_l - (\mu + \frac{\mu_{tl}}{\sigma_k}) \nabla k_l)) = \alpha_l (P_{kl} - \rho_l \varepsilon_l) + T_{\mathrm{lg}}^{(k)} \tag{22}$$

$$\nabla \cdot (\alpha_l \rho_l \mathbf{u}_l \varepsilon_l - (\mu + \frac{\mu_{tl}}{\sigma_\varepsilon}) \nabla \varepsilon_l)) = \alpha_l \frac{\varepsilon_l}{k_l} (C_{\varepsilon 1} P_{kl} - C_{\varepsilon 2} \rho_l \varepsilon_l) + T_{\mathrm{lg}}^{(\varepsilon)} \tag{23}$$

where $C_{\varepsilon 1}$, $C_{\varepsilon 2}$, σ_k, σ_ε are turbulence model constants, default values being 1.44, 1.92, 1.0 and 1.3 respectively. P_{kl} is the turbulence production due to viscous production in the liquid. $T_{\mathrm{lg}}^{(k)}$ and $T_{\mathrm{lg}}^{(\varepsilon)}$ represent additional source terms to account for turbulence production by bubbles following the model of Smith [30] and Olmos *et al.* [23].

Electro-magnetic effects are included through the Lorentz force (Equation 13), which is calculated from the magnetic field obtained from the metal-pad model in section 3.1 and the current density, **J**.

3.3.1 Electrical current model

The electrical current density at the anode surface is needed for the anode reaction equation (3) and cathode reaction equation (4) in the alumina distribution model, for the Lorentz force in the momentum equation (21) and for gas generation at the anode surface. Equations (10) and (11) show the relationship between current distribution, cell voltage and bath electrical conductivity. Bath conductivity is a function of gas holdup in the ACD and alumina concentration. Thus the local voltage and current are strongly coupled to the bath flow and the alumina reduction reactions in the alumina distribution models. In earlier work (Feng *et al.* [10][11][12][13], Witt *et al.* [35][36]) the current density was assumed uniformly distributed over the anode base and equally distributed to each anode. Similarly electrical conductivity and viscosity were assumed to be constant.

In this work the model is extended to solve for the current density and thus account for current density variations between anodes and across the anode surface based on gas holdup, anode age and cell resistance. The electric current distribution is obtained by first solving the scalar potential equation (11), without the induced current term, from which the current density, **J**, is found from equation (10), neglecting the B-field.

The equations are solved as a mixture of user defined scalar equations in ANSYS/Fluent R15.0 with the electrical conductivity calculated from the liquid conductivity calculated from species concentration (Hives *et al.*, [16]) and liquid volume fraction:

$$\sigma = \sigma_{bath}\, \alpha_l^{\,1.5} \tag{24}$$

This current density is then used with the magnetic field obtained from the metal pad model to calculate the Lorentz force for addition into the momentum equations (21).

Boundary conditions set for the electric current model are that the metal pad surface is at a voltage of 0 Volts and that the total cell current is fixed, for example at 300,000 A. The approach is to set a fixed cell current while allowing the voltage and current distribution through the multiple anodes to adjust, and is as follows:

1. An initial guess of the cell voltage is made and the voltage over the anode surface set,
2. Electrical conductivity is calculated based on temperature, composition, gas holdup,
3. The scalar potential equation is solved for one iteration,
4. At the end of the iteration, current through the anode base and sides is calculated.

5. An adjustment to the cell voltage is made based on the difference between the target cell current and the actual cell current.
6. Steps 2 to 6 are repeated until the model converges to a fixed cell voltage that satisfies the target cell current.

Electrical conductivity and bath viscosity are based on the species concentration and the liquid volume fraction; see Hertzberg *et al.* [15] and Hives *et al.* [16].

3.3.2 Geometry and boundary conditions

Geometry for the bath flow model was based on a Hydro Aluminium HAL300 cell and is shown in Figure 5. Cell length is 11.7 m with a width of 3.7 m and a bath depth of approximately 200 mm that varies due to heaving of the metal pad. Note that the metal layer is not included in the model, but its topology and velocity field is predicted by the metal pad model, with cell geometry, cathode current density profile and magnetic fields corresponding to the current cell design.

The full industrial cell has 30 anodes, each of length 1.5 m and width 0.7 m, which are included in the model. Each new anode has two 15 mm wide slots that are consumed during operation. Anode consumption also causes curvature of the anode edges that is accounted for with a 90 mm radius. Side and end channels are 200 mm in width but are narrower in practice due to formation of a frozen ledge, a typical ledge profile is included in the geometry. The geometry is meshed using ANSYS ICEM to give a final mesh of two million hexahedral cells. Particular effort was expended to ensure good quality cells with a minimum cell orthogonality of 0.4 and a maximum aspect ratio of 21.

The metal pad model described in section 3.1 predicts the shape of the metal-bath interface under the influence of the electro-magnetic field. Wang *et al.* [34], for a full cell, and Einarsrud [9], for a single anode water model, have used three phase CFD simulations to show that bubble flow under the anode can influence the metal pad shape. In [34] the electric and magnetic fields were calculated assuming rectangular anodes with a horizontal base combined with a fixed horizontal interface between the metal and bath layers. These fields were then interpolated onto their three phase model again with rectangular anodes. In their work the implied assumption is that changes in the metal-bath interface have no effect on the electric and magnetic fields. As shown by [34] the metal pad shape is complex and due to consumption of the carbon anodes by the electro-chemical reaction the shape of the anodes is also complex matching that of the metal-bath interface [39] so as to maintain a near constant voltage drop across the ACD. A consequence of the metal pad heave is that anode bases are

not horizontal and by buoyance forces the bubble flow along the anode base this greatly affected. Including the full MHD solution within a three phase flow model while capturing all the complex geometry and physical interactions is beyond current computing resources. In our work we have chosen to calculate the detailed bubble-cryolite flow separate from the metal pad so that effects of complex anodes profiles and metal pad heave on the current distribution and bubble flow can be accounted for with readily available computing resources. To account for the effect of bubble flow on the metal pad model we are developing an approach to take gas-liquid drag forces from the bath flow model and imposing these as body forces into the metal pad model.

When a new anode is placed into the cell, the anode has two slots. The anode and thus the slots are reduced in depth as the anode is consumed, hence the slot depth for each anode depends on the age of the anode that in turn is a function of the anode changing cycle. This variation in slot depth can be seen in Figure 5 and ranges from slots that extend beyond the top of the bath to slots that have been completely consumed. Gas enters the model through the anode base and sides with the mass flow rate determined from the predicted current density on the anode surface. Gas leaves the domain through the top free surface coloured green via a degassing boundary condition. At walls it is not practical to resolve the boundary layer, so the scalable wall function option in Fluent is used. Anode and cell side walls are treated as no-slip walls with a zero velocity. As predicted by the metal pad model the metal pad surface has a velocity driven by the MHD forces thus the predicted metal pad velocity is applied at the surface of the metal pad.

3.3.3 Bath Flow Model Implementation

The bath flow model is implemented in ANSYS FLUENT 15.0 with user-defined functions used to add and remove gas mass from the model. Also, the bubble induced turbulence, drag model, the momentum source term and fluid property dependence on temperature, species and volume fraction are implemented through user defined functions. Inter-phase coupling of the momentum equations was handled using the coupled solver, and convective terms in the transport equations were discretised using the QUICK differencing scheme. To provide stability a pseudo-transient method with false time steps of 0.001 seconds was used.

Coupling between the electrical current model and the bath flow is very strong due to variations in gas holdup changing electrical resistance and anode surface current responsible for generating the bubbles. To solve the bath flow and current; solution of the bath flow equations was performed for 10 iterations. These were turned off and solution of the potential equation performed, with the

iteration procedure for anode currents noted above, until the potential equation converged to a residual of 0.00001. Solution of the bath flow model was obtained by iterating between the two sets of equations (solution of the scalar voltage potential and the bath fluid flow equations) until the system converged.

3.4 Alumina distribution model

Alumina distribution within the cells is important for cell efficiency and preventing anode effects. The alumina distribution model describes the transient distribution and consumption of alumina and other chemical species within the liquid bath. Using the bath flow information and an assumption of uniform reduction rate, a single scalar transport equation has previously been used to track the time variation of alumina within cells (Feng *et al.* [12]). Recently a six species electrolysis model for alumina reduction was developed by Witt *et al.* [36] and in this work has been coupled to the bath flow model by making bath properties such as density, electrical resistivity and viscosity functions of the local species concentrations.

3.4.1 Basic electrolysis reactions

The alumina reduction process is represented by a set of four electro-chemical equations that are used to predict the distribution of six chemical species (noted earlier in the bubble model description) within the liquid bath, cf. equations (1)-(4). To solve these reaction rates k_1, k_2, k_3, k_4, are required.

Dissolution of solid alumina particles into the bath is a complex process involving particle agglomeration, particle heating, freezing and remelting of solid layers of bath around agglomerates and phase transformation of γ to α alumina [2]. Heat transfer and mass transfer between the agglomerate and bath along with alumina moisture content and agglomerate size are the key factors controlling the dissolution rate. The first two rely on detailed bath flow, temperature, bath superheat and chemical composition information. A complete mathematical model of the dissolution process is not available in the open literature (cf. [2] and [37]). Complex models for a single alumina particle or agglomerate have been proposed, cf. Dassylva-Raymond et al. [2], but incorporation into a CFD model would require tracking for each agglomerate; information such as diameter, radial temperature distribution, frozen bath layer thickness and chemical composition. Such an approach would greatly add to the computational demands and is beyond the scope of the present work. This is further

complicated by the lack of mechanistic models for agglomerate formation or detailed measurements of agglomerate size distribution.

An alternate approach using a population balance model for the agglomerate size in a forty anode cell was proposed by Zhan [37] using heat and mass transfer coefficients based on agglomerate size to calculate the dissolution rate. Agglomerates were divided into two sizes, large and small, with each size represented by twelve size classes. To make the problem manageable they assumed a fixed bath temperature and superheat. Gas flow was not directly predicted but was imposed through force terms calculated in a separate simulation. To stabilise the model time steps on the order 0.001 s were used. Using this approach [37] were able to simulate 144 s or one to two feeding cycles.

Our aim is to model thousands of feeding cycles and the resultant changes in alumina concentration thus we need to simulate up to 20,000 s therefore complex approaches such as [2] and [37] are unaffordable and to justify their level of complexity require prediction of the bath temperature and superheat distribution in the cell. Frovlov *et al.* [14] carried out dissolution experiments for both a modified and a typical industrial bath chemistry at a bath temperature of 960°C and over a range of dissolved alumina concentrations. For the industrial bath composition their measured rates are comparable to those of [21].

For the alumina dissolution rate in the current model we have used the industrial bath chemistry data reported by Frovlov *et al.* [14] as this is experimentally based and includes some mass transport effects through dissolved alumina concentration. To incorporate the data into the model two straight lines are fitted to their data, as shown in Figure 6, the following rate equation, as a function of the dissolved alumina mass fraction, $Y_{Al2O3dis}$, can be obtained:

$$k_1 = \max\left(0, 0.35 - \frac{0.35}{0.03} Y_{Al2O3dis}, 0.164 - \frac{0.164}{0.07} Y_{Al2O3dis}\right) \tag{25}$$

To limit the reaction in areas of very low undissolved alumina, the equation is modified to include the mass fraction of undissolved alumina, $Y_{Al2O3UnD}$:

$$k_1 = \left(1 - \exp\left(-500 Y_{Al2O3UnD}\right)\right) \max\left(0, 0.35 - \frac{0.35}{0.03} Y_{Al2O3dis}, 0.164 - \frac{0.164}{0.07} Y_{Al2O3dis}\right) \tag{26}$$

Where mass fractions (Y_i) are kg of specie *i* per kg of bath and the dissolution rate, k_1, is a volumetric rate [mol per second per m^3 of bath].

The equilibrium reaction rate is calculated assuming equilibrium of equation (2). Based on data from Solheim and Sterten [31] the equilibrium condition reported in Solheim *et al.* [32] is:

$$\frac{x_1^2}{x_2} = 11.3\exp(-2.63r) \tag{27}$$

where x_1 and x_2 are the molar fractions of $Na_2Al_2OF_6$ and $Na_2Al_2O_2F_4$ respectively with the units of number of mol of specie *i* per mol of bath, and *r* is the molar ratio (Cryolite Ratio) of NaF and AlF_3.

Using Faraday's law of electrolysis, reaction rates at the surface of the anode, k_3, and cathode, k_4, in equations (3) and (4), are based on the local current density, **J**, at the anode and cathode surfaces such that:

$$k_3 = \frac{\mathbf{J}_{Anode} \cdot d\mathbf{A}_{anode}}{4F} \tag{28}$$

and

$$k_4 = \frac{\mathbf{J}_{Anode} \cdot d\mathbf{A}_{cathode}}{4F} \tag{29}$$

Noting that *F* is Faraday's constant (96 485 [A s mol^{-1}]) and $d\mathbf{A}$ [m^2] is the cell face surface area of the anode and cathode (metal pad).

3.4.2 Model implementation

Transport of alumina and other chemical species is obtained by solution of transient mass fraction transport equations for the species of undissolved alumina, $Na_2Al_2O_2F_4$, $Na_2Al_2OF_6$, NaF, and AlF_3. Sodium (Na^+) mass fraction is also included in the model and is treated as a constraint on the mass fractions summing to one.

$$\frac{\partial(\alpha_l \rho_l Y_i)}{\partial t} + \nabla \cdot (\alpha_l \rho_l \mathbf{u}_l Y_i - (\Gamma_i)\nabla Y_i)) = S_i \tag{30}$$

Convection and diffusion terms in equation (30) are based on velocity, turbulence quantities and volume fractions from the steady state bath flow model. Source terms, S_i, are used to add feeding and as sources and sinks terms for reactions given by equations (1) – (4).

Key features of the alumina distribution model are:

- Transport of species is based on the steady state bath flow model,
- Alumina feeding varies in time and occurs at a number of locations,
- A fixed time of 10 seconds is assumed for particles from feeder to mix into the bath.

Alumina feeding occurs at the bath surface through five feeders located in the centre channel between anodes 2&17, 5&20, 8&23, 11&26 and 14&29 (cf. Figure 5). Each feeder operates at different times depending on the feeding cycle. Each feed is approximately 1 kg of alumina and feeding occurs approximately every 50 seconds.

Initial concentrations for the mass fractions are given in Table 2 and give a cryolite ratio of 2.2 from which the equilibrium condition for $Na_2Al_2OF_6$ and $Na_2Al_2O_2F_4$ can be determined. The same mesh used for the bath flow model is used and flow variables are initialised using results from the bath flow model. QUICK is again used as the discretisation scheme for the convective terms with a first order implicit discretisation of the transient terms. The alumina distribution model was run for a time of 20,000 seconds with 1 second time steps and a convergence criterion of $1x10^{-7}$ for the mass fraction equations.

4 Coupling of models

4.1 General assumptions and connections

In complex processes, a large number of variables are involved which leads to fluctuations distributed in a Gaussian manner. Both coupling and dissipation in the system drive a system far from equilibrium and may establish a new space-time organisation (Prigogine [25]). This new space-time organisation is an emergent property of a system where the individual component interactions result in a macroscopic behaviour, called self-organising criticality.

A pragmatic approach to investigate and simulate these complex processes is to separate the phenomena and try to find correlations, 1- or even 0-dimensional representations, and couple these. Especially in industrial approaches where fast or even real-time information for control and stirring is needed, this pragmatic industrial approach needs to be applied, (Zoric *et al.,* [38]).

To achieve these simplified representations a detailed physical and chemical modelling approach will be used to increase the insight and derive the effective principles. Additionally, scaling of main process phenomena and their coupling behaviour can be used to structure a modelling environment for the aluminium electrolysis process.

4.2 Scales in the aluminium production process

The dimensions of the main process phenomena span over 6 decades in length and 8 decades in time preventing an integrated simulation approach covering all given phenomena with the computational working conditions in research institutes and industry. The different zones in the length/time diagram

in Figure 7, indicate possible separate phenomena that can be solved in separate modelling approaches and then coupled back in to the next simulation level.

Magnetic effects are established quite fast and remain stable, based on the constant system current in the overall potlines, until the next operational impact such as metal tapping or anode changes, which occur every 24 hours. This implies that the magnetic environment can be predicted with a steady state approach, with the predicted magnetic state then applied to the flow phenomena as a geometrical initial condition and static magnetic field.

The small reaction-initiated gas bubbles of less than 1 mm cannot be simulated in the dimension of a 1500 mm long anode or even 30000 mm long cell, as it would require immense computing capacity to handle the millions of required elements for sufficient resolution. Therefore a mathematical model, such as a population balance model, can be used for bubbles until the bubble length scale reaches the scale of the simulation domain mesh size. At this point the gas is then transferred into a volume of fluid (VOF) bubble flow model, allowing the application of surface tension and wetting conditions into this transient flow behaviour.

The bubble related draft flow and turbulent viscosity can be applied in the next approach of a full cell bath flow model as time averaged volume sources, predicting the stable steady state flow pattern in the cell. Finally, this overall flow pattern can be applied in a transient alumina distribution model (ADM) for predicting the transient feeding and consumption behaviour of the electrolysis process.

4.3 Primary coupling in the aluminium production process

Figure 8 gives an overview of the different coupling mechanisms investigated here. There is a straightforward coupling from the magnetic toward the bubble part, as long as the geometrical conditions of metal pad and anode shape remain unchanged. This impact is marked with straight arrows. The impact of geometrical changes is marked with dashed arrows.

Comparison between laboratory and industrial cell measurements, and simulations, indicate that some basic coupling mechanisms are missing in a two-phase flow without the bubble surface physics to establish typical intrinsic frequencies, cf. Bilek *et al.* [1] and Einarsrud [5]. This reflects the level of coupling if only the MHD and bubble induced forces are considered in the first two columns of Figure 8.

When adding the chemical species and their impact on bulk and surface properties (see dotted line in Figure 8) the coupling is extended from the bottom of the flow impact row back to the top initiating coupling loops. This is a main effect generating realistic flow and process behaviour.

5 Results

5.1 Results from metal flow model

5.1.1 Verification of approach

Comparison of metal pad height by modelling and measurements is quite a challenging task for the harsh conditions in an industrial smelting process. With the steel rod method the flow direction and speed of the bath phases can only be indirectly measured by the dissolved shape of a steel rod, cf. for instance Severo *et al.* [27], submerged into the liquid part of the cell for a defined period. The comparison between simulation results and measurements for one test case as shown in Figure 9 is quite good, based on the simple measurement approach. More accurate measurement methods need to be developed to further increase the accuracy of the modelling approach.

5.1.2 Metal pad profile and flow pattern

The steadiness of the transient simulation results is estimated by averaging the transient data over a period of 4s. It is found that the simulations reach quasi-steady state after 240s of simulation time (6000 time steps). The results presented in this paper are the simulation data at 240s or 6000th time step.

Figure 10 (a) shows the deformation of bath-metal interface at the 6000th time step predicted by the model. The metal pad heaves upward at the reduction cell center, and downward at the position near the two ends. The total metal height difference inside the cell is about 11cm. The fluid velocity distribution on the metal pad predicted by the simulation is shown in Figure 10 (b). There are several flow vortices on the metal pad. The maximum velocity in the metal layer is about 26 cm/s and the mean velocity about 14 cm/s. The metal profile and flow velocity at the metal profile are used for the boundary condition for the bath flow model.

5.2 Results from mesoscale bubble model

5.2.1 Verification of approach

Suitable measurement techniques for the electrolyte flow pattern and species concentrations are lacking for industrial cells, owing to the harsh environment. In order to obtain data for validation, laboratory scale electrolysis experiments have been performed (see Eick et al. [3]), aiming to describe bubble induced voltage fluctuations under various operating conditions on a 10 by 10 cm carbon anode.

A subset of the experimental conditions have been simulated using the proposed approach, as described in Einarsrud *et al.* [8]. A snapshot from a simulation with current density 0.8 A/cm^2 (uniformly distributed on the cathode surface), 4 cm ACD and 2^o anode inclination is shown in Figure 11. Qualitatively, the depicted topology of the gas bubble layer corresponds well to that observed in recent water model experiments performed by Simonsen et al. [29].

A comparison of simulated and measured voltage curves for the same conditions is shown in Figure 12. The simulated voltage signal is characterized with a frequency of 0.54 Hz and an amplitude of 97 mV, corresponding well to experimental values of 0.44 Hz and 115 mV.

All simulated results (amplitude (A) vs. frequency (f)) are compared to experimental results in Figure 13, with a least square fit of the form:

$$A = \frac{a}{f - b} + c\,, \tag{31}$$

based on the *experimental* data as proposed by Wang and Taberaux [33]. Although the simulated results show somewhat higher frequencies (i.e. larger bubble velocities) and lower amplitudes (i.e. smaller bubble sizes) than the corresponding experiments, indicating that surface phenomena such as coalescence and adhesion are under predicted in the simulations, all simulated results are nevertheless within the expected range and follow the experimental trend to an acceptable level.

5.2.2 Single anode simulations

Typical simulation results of anode bubble flow with variation of anode tilting and current density of 0.8 and 1.1 A cm^{-2} are given in Figure 14a-c for an industrial sized anode with active area 1.5 by 0.7 m. Anode tilting is used to represent different shapes of the metal pad profile that result in anode shaping. The tilting is such that buoyant gas bubbles tend to move towards the right side of the anode for each of the cases simulated, corresponding to the centre channel in a real cell. With increasing current density, the gas accumulation is increased, as more gas is being produced (cf. case a and case

b in Figure 14), while with increasing the tilting angle the gas accumulation is reduced (cf. case a and c in Figure 14).

5.3 Results from full cell bath flow model

Applying the metal pad profile and speed from the first approach allows detailed MHD effects to be included into the full cell bath flow model. Work is underway to also apply the bubble draft and turbulent viscosity from the meso-scale model into the bath flow model so that detailed bubble effects are also included in the full cell. At present this information is derived from model validation against laser measurements in air-water models (Feng *et al.* [11][13]).

Streamlines for the coupled flow field of the full simulation domain are plotted in Figure 15(a) and velocity vectors, as shown in Figure 15(b), in the centre of the anode cathode distance (ACD) on a surface parallel to the metal pad and 20 mm above the metal pad. Typical speed is about 10-20 cm s^{-1} and the flow fields show that for anodes with consumed slots there is substantially stronger cross flow.

Gas hold up under and beside the anodes is shown on a vertical plane along the centre of anodes 8 and 13 in Figures 16. Bath flow in the centre and side channels is also shown in Figure 16. In both side channels and the centre channel bubble driven circulation occurs that is controlling the back flow of bath into the ACD.

5.4 Results from alumina distribution model

The bath flow pattern calculated above contains detailed MHD and bubble effects obtained by interlinking MHD effects from the metal pad model into the bath flow model and allows for prediction of species distribution within the cell.

Mass fractions for the undissolved alumina species are given in Figure 17, which clearly show the five feeding points and distribution based on advection, diffusion and reduction. As alumina is fed to the top of the centre channel, undissolved alumina mass fraction is highest there. Undissolved alumina is then transported from the centre channel via the anode gaps to under the anodes by the bath flow. Whilst the transient feeding scenario complicates interpretation of the results, a trend in the variation in alumina concentrations can be seen with lower alumina concentration at the cell ends than near the cell centre; as is evident, in differing degrees, at time instants 3600, 7200 10000 and 12000 seconds. For a similar 300kA cell with 30 anodes, Moxnes *et al.* [22], found by operational tests that cell performance was improved when feeding was increased towards the ends and reduced

near the cell centre thus supporting model predictions of lower alumina concentrations towards the cell ends.

The feeding scenario applied in the model is taken from industrial cell operation, showing the impact of alternating under- and overfeeding periods on undissolved alumina over 20000s operation period, see Figure 18a. Alumina feeding in the model, in parallel to cell operation, is based on single alumina shots occurring approximately every 50 seconds from each of the five different feeders, as indicated in the magnification of Figure 18a.

The model now allows investigation of the species concentration in the cell and study of the impact of the driving forces of magnetic field and bubble draft. Starvation of alumina in specific areas can be identified and the feeding adjusted. This transient feeding and consumption process causes species fluctuations during the feeding cycle shown in Figure 18b. The equivalent alumina concentration is used to determine local properties in the bath (as described in sections 3.2.5 and 3.3.1) and is determine by calculating the total molar concentration of the alumina species, from this the equivalent mass of alumina at each point is calculated. From this the equivalent alumina mass fraction is calculated, with its change in concentration over time plotted in Figure 18b.

In the first 3000 seconds, the system is adjusting to an equilibrium state. In comparison to the under- and overfeeding cycle, the relevant oxyfluoride concentration ($Na_2Al_2OF_6$, $Na_2Al_2O_2F_4$) for the anodic reaction is quite stable during the entire period. Unfortunately existing measurement techniques are not available for model verification, but the conservation of species in the model, proven dependencies of bath properties from species concentration and qualitative agreement between predicted alumina distributions and operational feeding tests gives high confidence.

6 Conclusions and future work

A simulation environment has been developed where four different simulation approaches to predict the aluminium electrolysis process can be coupled. The MHD metal pad prediction, the multiscale and multi-field model for anodic bubble flow and the full cell bath flow approach allowing for bath chemistry and variable bath properties have been presented. Results have been verified by comparison to available laboratory- and industrial scale experiments, showing good correspondence in the range of measurement capabilities.

Coupling of the models is demonstrated by using information from the metal pad model and bath flow model to obtain information regarding alumina distribution in the cell. The reaction pathway

developed for the model shows expected behaviour based on single anode current measurements. Applications of the modelling approach include improved feeding strategies for reducing anode effects and supporting selection of effective feeding positions.

With prediction of the transient local alumina concentration more opportunities in process control are given by adjusting the individual feeding frequency of each single feeder in dependency to the current anode setting cycle. Short comings in alumina at specific areas of cell during amperage increase can be predicted and measures taken [22].

Future work will involve improved description for alumina dissolution, for instance by introducing PBM-concepts also for alumina particles and agglomeration as in [2, 37], thermo-electrical and magnetic models, allowing for more realistic calculations of magnetic fields, and increasing the extent of coupling between the sub-models developed. Special attention will be given to usage of the meso-scale bubble model as a numerical lab in order to establish new and extend the validity of existing correlations for gas-bath momentum exchange and to impose bubble drag forces calculated in the bath flow model into the metal pad model to allow bubble effects on the metal pad to be accounted for.

Finally, it should be stressed that further experiments and new measurement techniques are needed in order to verify and validate the coupled approach, for instance by dedicated cell voltage measurements combined with bath sampling at specific points of interest which can be pinpointed by the models proposed in the current work.

7 Acknowledgment

The present work was supported by two projects financed by Hydro Aluminium and the Research Council of Norway. Permission to publish the results is gratefully acknowledged.

This paper is an extension of a conference paper that was presented at the Eleventh International Conference on CFD in the Minerals and Process Industries (CFD2015), and was nominated for invitation into the CFD2015 Special Issue of Applied Mathematical Modelling based on its designation as a high-quality paper of relevance to the modelling of fluids-based systems.

8 References

[1] M. M. Bilek, W. D. Zhang, F. J. Stevens, Modelling of Electrolyte Flow and Its Related Transport Processes in Aluminium Reduction Cells, in: M. Gilbert, P. Tremblay & E. Ozbeck (Eds.), Light Metals, 1994, TMS, Warrendale P. 1994, pp.323-321.

[2] V. Dassylva-Raymond, L. I. Kiss, S. Poncsak, P. Chartrand, J.-F. Bilodeau, S. Guérard, Modelling the behaviour of alumina agglomerate in the Hall-Heroult process, in: J. Grandfield (Ed.), Light Metals, 2014, TMS, Warrendale P. 2014, pp. 603-608.

[3] I. Eick, A. Klaveness, C. Rosenkilde, M. Segatz, H. Gudbrandsen, A. Solheim, E. Skybakmoen, K. E. Einarsrud, Voltage and Bubble release behaviour in a laboratory cell at low anode-cathode distance", 10th Australasian Aluminium Smelting Technology Conf. (AASTC), Launceston, Tasmania, 2011.

[4] I. Eick and K.E. Einarsrud, Bubble release noise and self-organized criticality in aluminium electrolysis, 11th Australasian Aluminium Smelting Technology Conf. (AASTC), Dubai, 6-11 December 2014.

[5] K.E. Einarsrud, A Treatise on Interpolar Transport Phenomena, PhD Thesis 201, NTNU: Trondheim, Norway, 2012.

[6] K. E. Einarsrud and S.T. Johansen, Modelling of Bubble Behaviour in Aluminium Reduction Cells, Progress in Computational Fluid Dynamics, 12 (2) (2012), 119-130.

[7] K. E. Einarsrud, S. T. Johansen, I. Eick, Anodic Bubble Behaviour in Aluminium Reduction Cells, in: C.E. Suarez (Ed.), Light Metals, 2012, TMS, Warrendale P. 2012, pp. 875-880.

[8] K. E. Einarsrud, I. Eick, P. J. Witt, A. Solheim, Y. Q. Feng, Impact of Variable Bath Chemistry and Wetting on Gas Bubble Flow in Aluminium Reduction Cells, in: M. Hyland (Ed.), Light Metals, 2015, TMS, Warrendale P. 2015, pp., 649-654.

[9] K.E. Einarsrud, The Effect of Detaching Bubbles on Aluminium-Cryolite Interfaces: An Experimental and Numerical Investigation, Metall. and Materi. Trans B (2010), 41B, 560-573.

[10] Y.Q. Feng, M. Cooksey and M.P. Schwarz, CFD Modelling of alumina mixing in aluminium reduction cells, in: J.A. Johnson (Ed.), Light Metals, 2010, TMS, Warrendale P. 2010, pp. 455-460.

[11] Y.Q. Feng, W. Yang, M. Cooksey and, M.P. Schwarz, Development of Bubble Driven Flow CFD Model Applied for Aluminium Smelting Cells, J. Comp. Multiphase Flows, 2 (3) (2010), 179-188.

[12] Y.Q. Feng, M. Cooksey and, M.P. Schwarz, CFD Modelling of alumina mixing in aluminium reduction cells, in: S.J. Lindsay (Ed.), Light Metals, 2011, TMS, Warrendale P. 2011, pp. 543-548.

[13] Y.Q. Feng, M.P. Schwarz, W. Yang and M.A. Cooksey, Two-phase CFD model of the bubble-driven flow in the molten electrolyte layer of a Hall-Héroult aluminum cell, Metall. and Materi. Trans B (2015), 46:1959-1981.

[14] A. V. Frolov, A. O. Gusev, Y. P. Zaikov, A.P. Khramov, N. I. Shurov, O. Y. Tkacheva, A. P. Apisarov, V. A. Kovrov, Modified alumina-cryolite bath with high electrical conductivity and dissolution rate of alumina, in: M. Sorlie (Ed.), Light Metals, 2007, TMS, Warrendale P. 2007, pp. 571-576.

[15] T. Hertzberg, K. Tørklep, H. A. Øye, Viscosity of molten NaF-AlF_3-Al_2O_3-CaF_2 mixture; selecting and fitting models in a complex system, in:C.J. McMinn (Ed.), Light Metals, 1980, TMS, Warrendale P. 1980, pp. 159-170.

[16] J. Hives, J. Thonstad, Å. Sterten, P. Fellner, Electrical conductivity of molten cryolite-based mixtures obtained with a Tube-Type cell made of Pyrolytic boron nitride, in: M. Gilbert, P. Tremblay & E. Ozbeck (Eds.), Light Metals, 1994, TMS, Warrendale P. 1994, pp. 187-194.

[17] J. Hua, C. Droste, K. E. Einarsrud, M. Rudshaug, R. Jorgensen, N.-H. Giskeodegard, Revised Benchmark Problem for modelling of metal flow and metal heaving in reduction cells, in: J. Grandfield (Ed.), Light Metals, 2014, TMS, Warrendale P. 2014, pp. 691-695.

[18] M. Ishii, N. Zuber, Drag coefficient and relative velocity in bubbly, droplet or particulate flows, AIChE Journal, 25 (1979), 843-855.

[19] B. Lafaurie, C. Nardone, R. Scardovelli, S. Zaleski, G. Zanetti, Modelling Merging and Fragmentation in Multiphase Flows with SURFER, Journal of Computational Physics, 113 (1) (1994), 134-147.

[20] M. Lopez De Bertodano, Turbulent bubbly flow in a triangular duct, Ph.D. Thesis, Rensselaer Polytechnic Institute, New York, 1991.

[21] Z. Lubyova, V. Danek, Control Mechanism for Alumina Dissolution in Cryolite Melts, Chemicke zvesti (1995), 49(2), 59-63.

[22] B. Moxnes, A. Solheim, M. Liane, E. Svinsås, A. Halkjelsvik, Improved cell operation by redistribution of the alumina feeding, in: G. Bearne (Ed.), Light Metals, 2009, TMS, Warrendale P. 2009, pp. 461-466

[23] E. Olmos, C. Gentric, N. Midoux, Numerical description of flow regime transitions in bubble column reactors by a multiple gas phase model, Chemical Engineering Science, 58 (2003), 2113-2121.

[24] S. B. Pope, Turbulent Flows, Cambridge University Press, 2000.

[25] I. Prigogine, Exploring Complexity, European Journal of Operational Research, 30 (1987), 97-103.

[26] M. Segatz, C. Droste and D. Vogelsang, Magneto-hydrodynamic effect of anode set pattern on cell performance, in: R. Huglen (Ed.), Light Metals, 1997, TMS, Warrendale P. 1997, pp. 429-435.

[27] D.S. Severo, V.Gusberti, A. F. Schneider, E. C. Pinto, V. Potocnik, Comparison of various methods for modeling the metal-bath interface, in: D.H. DeYoung (Ed.), Light Metals, 2008, TMS, Warrendale P. 2008, pp. 413-418.

[28] T. H. Shih, W. W. Liou, A. Shabbir, Z. Yang, J. Zhu, A new k-e Eddy-Viscosity Model for High Reynolds Number Turbulent Flows – Model Development and Validation, Computers & Fluids, 24 (1995), 227-238.

[29] A. J. Simonsen, K. E. Einarsrud, I. Eick, The impact of bubble-bubble interaction on anodic gas release; a water model analysis, in: M. Hyland (Ed.), Light Metals, 2015, TMS, Warrendale P. 2015, pp. 795-800.

[30] B. L. Smith, On the modelling of bubble plumes in a liquid pool, Applied Mathematical Modelling, 22 (1998), 773-797.

[31] A. Solheim and A. Sterten, Activity of Alumina in the System NaF-AlF_3-Al_2O_3 at NaF/AlF_3 Molar rations ranging from 1.4 to 3, in: C.E. Eckert (Ed.), Light Metals, 1999, TMS, Warrendale P. 1999, pp. 445-452.

[32] A. Solheim, H. Gudbrandsen, A. M. Martinez, K. E. Einarsrud, I. Eick , Wetting between carbon and cryolitic melts. Part II: Effect of bath properties and polarization, in: M. Hyland (Ed.), Light Metals, 2015, TMS, Warrendale P. 2015, pp. 671-676

[33] X. Wang, A. T. Taberaux, Anodic phenomena - Observations of anode overvoltage and gas bubbling during aluminium electrolysis, in: R.D. Peterson (Ed.), Light Metals, 2000, TMS, Warrendale P. 2000, pp. 239-247.

[34] Q. Wang, B. Li, Z. He, N.X. Feng, Simulation of Magnetohydrodynamic Multiphase Flow Phenomena and Interface Fluctuation in Aluminium Electrolytic Cell with Innovative Cathode, Metall. and Materi. Trans B (2014), 45B, 272-294.

[35] P.J. Witt, Y.Q. Feng, I. Eick, M.P. Schwarz, Modelling bubble flow with CFX and Fluent for aluminium reductions cells, 9th Int. Conf. on CFD in the Mineral and Process Industries, CSIRO, Melbourne, Australia, 10-12 December 2012.

[36] P.J. Witt, Y.Q. Feng, G.A. Snook, I. Eick, M. Cooksey, A Six Chemical Species CFD Model of Alumina Reduction in a Hall-Heroult Cell, Progress in Applied CFD, Eds, J.E. Olsen and S.T. Johansen, Norway, SINTEF Academic Press, 2015, 39-48.

[37] S. Zhan, M. Li, J. Zhou, J. Yang, Y. Zhou, CFD simulation of dissolution process of alumina in an aluminium reduction cell with two-particle phase population balance model, Applied Thermal Engineering 73 (2014), 805-818.

[38] J. Zoric, S. T. Johansen, K. E. Einarsrud, A. Solheim, On Pragmatism in Industrial Modeling, Progress in Applied CFD, Eds, J. E. Olsen and S. T. Johansen, Norway, Norway SINTEF Academic Press, 2015, 9-24.

[39] J. Zoric, J. Thonstad, T. Haarberg, The Influence of the Initial Shape and Position of an Anode and the Curvature of the Aluminum on the Current Distribution in Prebaked Aluminum Cells, Metall. and Materi. Trans B (1999), 30B, 341-348.

Figures and Tables

Table 1: Material Properties used for metal pad model.

Material property	Unit	Electrolyte	Liquid Aluminum
Density	kg/m^3	2070	2270
Viscosity	mPa s	1.25	2.5
El. conductivity	$S\ m^{-1}$	250	3.0E6

Table 2: Initial Species mass fractions in the model.

Al_2O_3	$Na_2Al_2O_2F_4$	$Na_2Al_2OF_6$	Na	NaF	AlF_3
0.025[1]	0.044[2]	0.084[2]	0.070[2]	0.420[2]	0.382[2]

[1] Mass fraction of total liquid phase
[2] Mass fractions of dissolved species

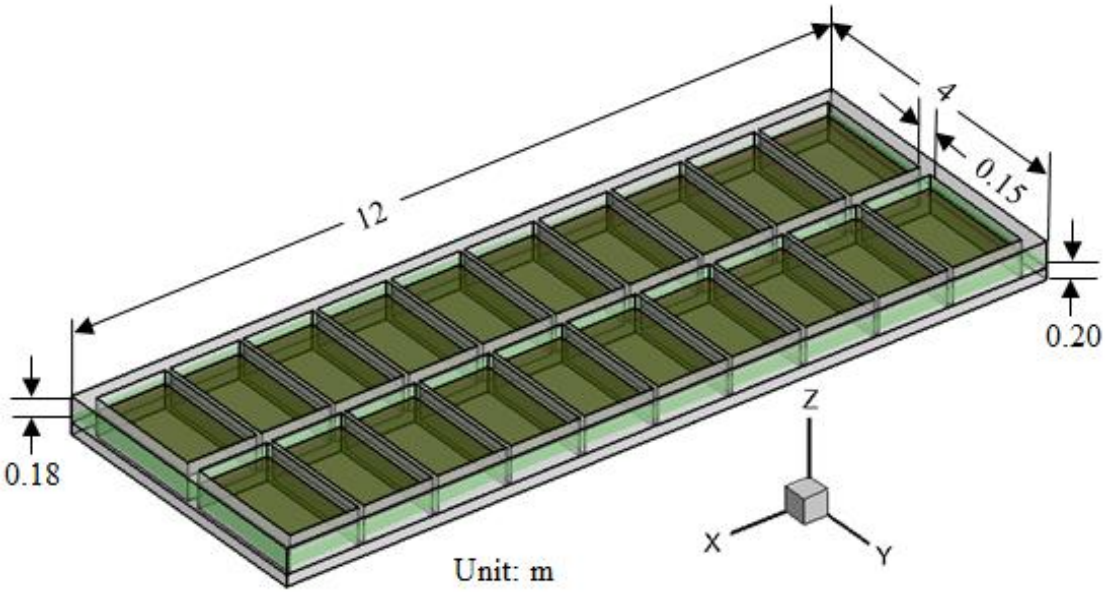

Figure 1: Geometry of the box model for metal pad profile prediction in an alumina reduction cell.

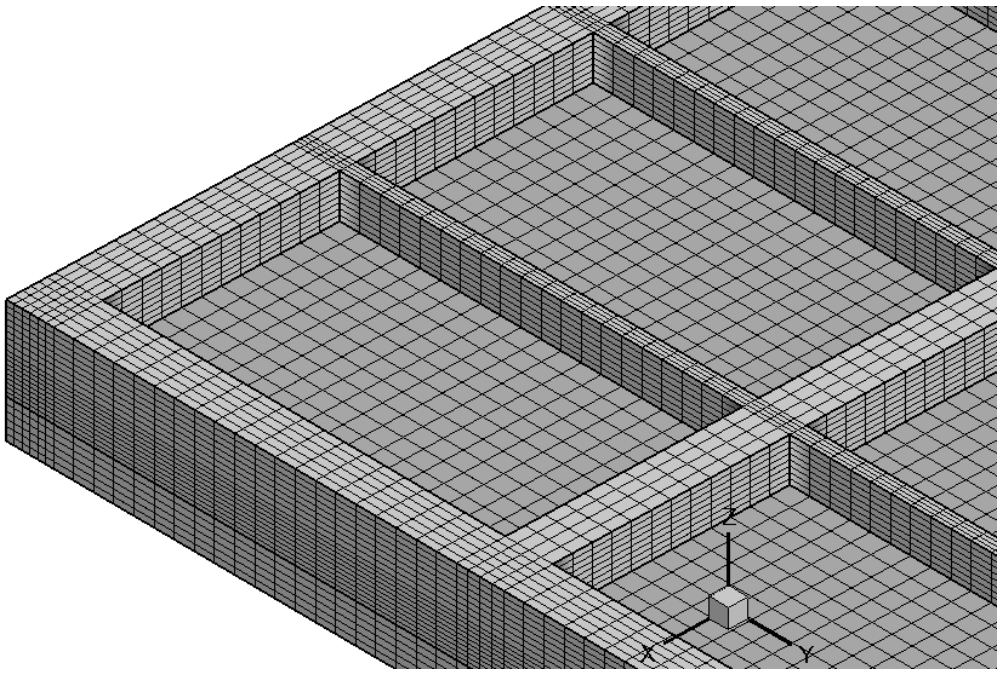

Figure 2: CFD mesh used for the numerical simulation of metal pad profile.

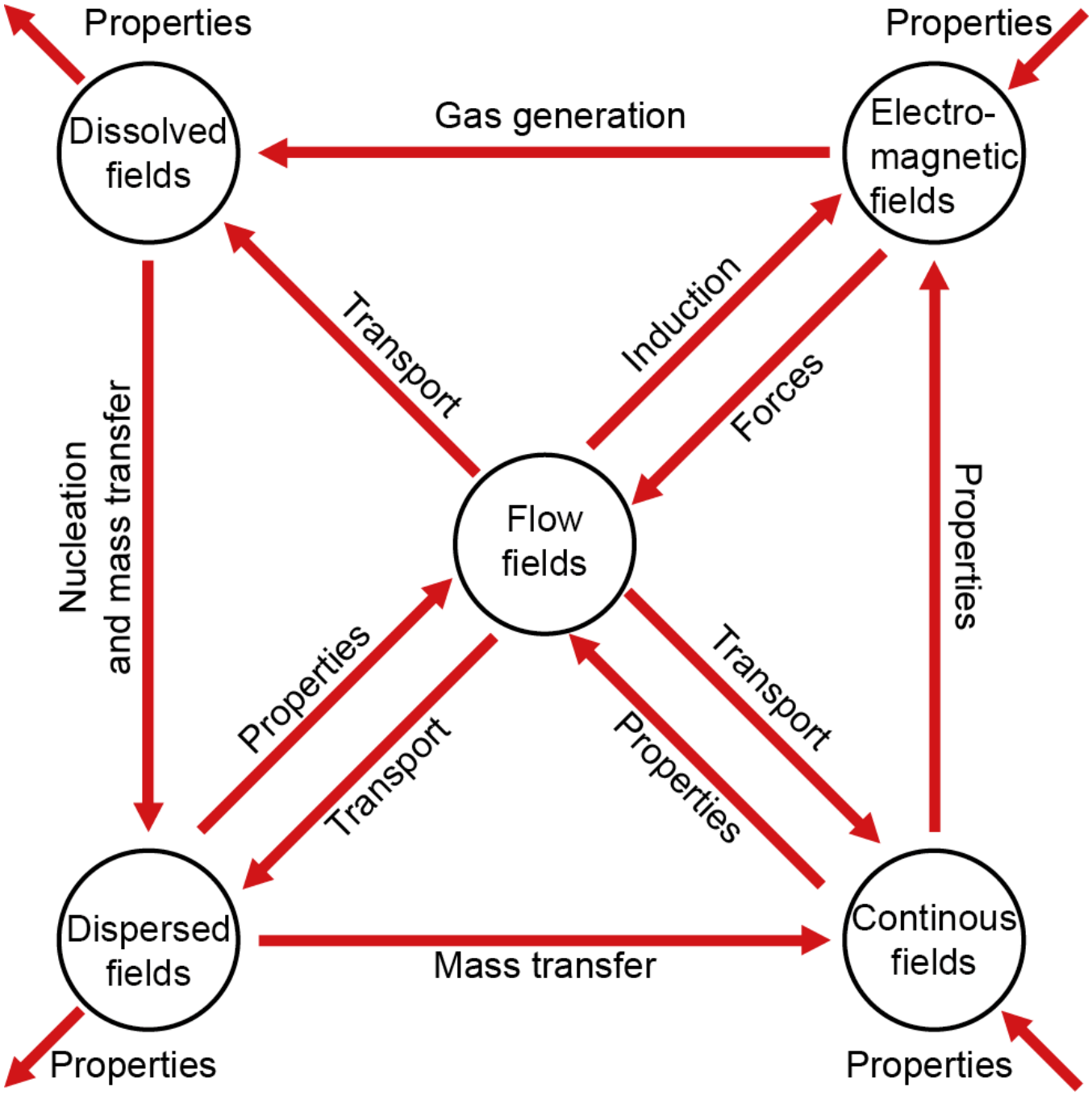

Figure 3: Overview of fields in mesoscale framework and their interactions.

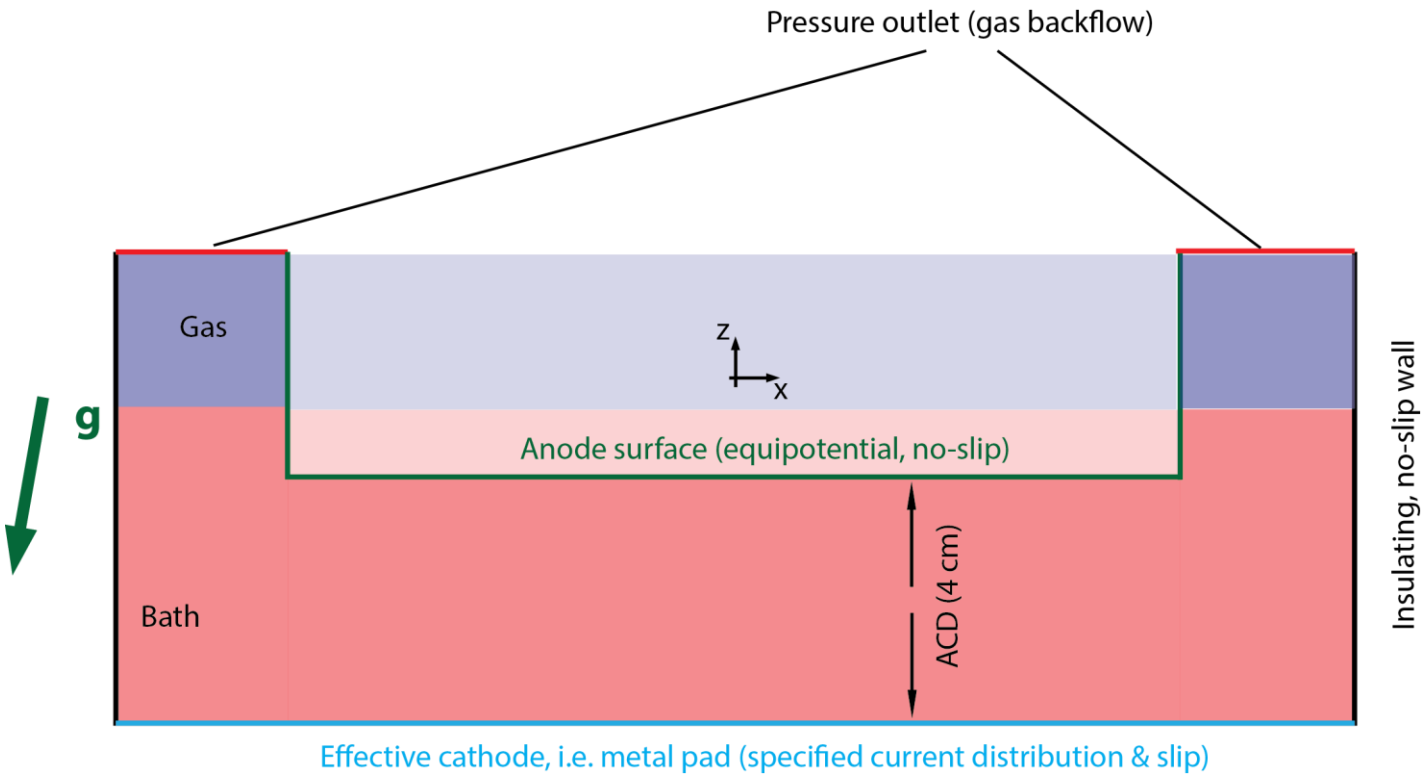

Figure 4: 2D schematic of mesoscale model.

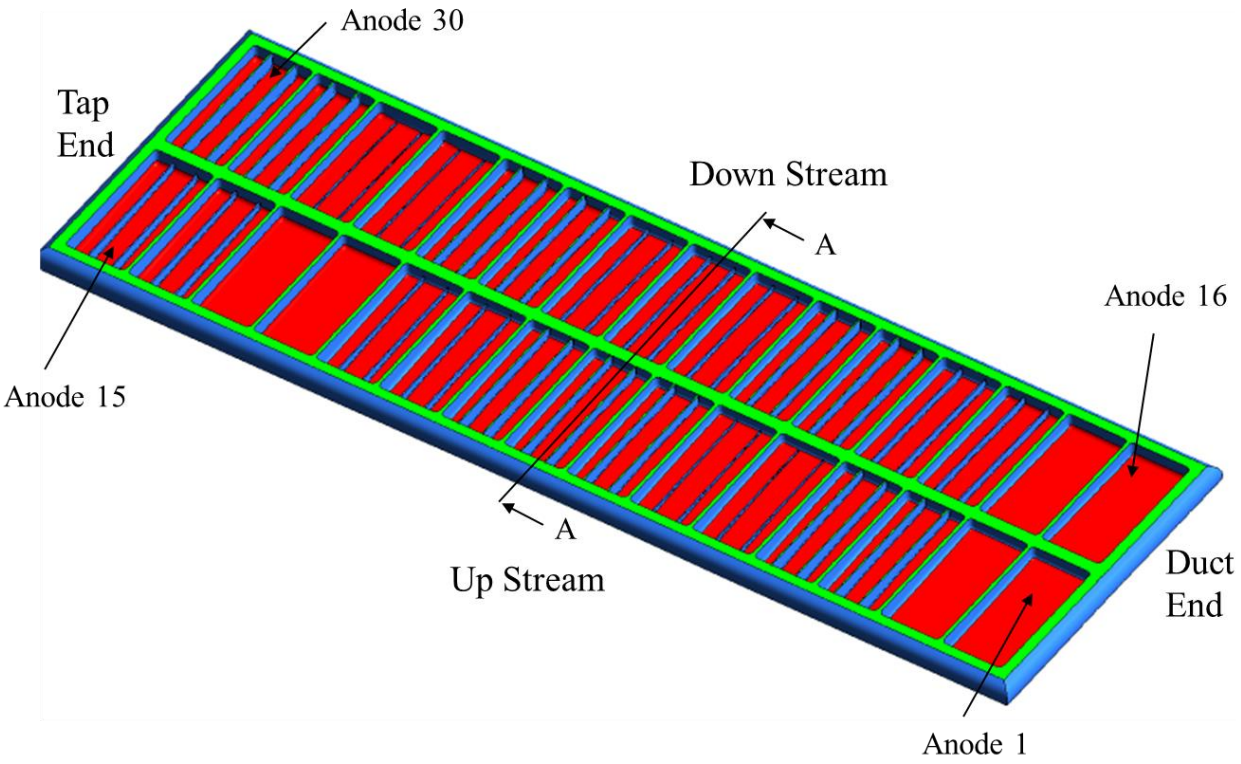

Figure 5: Full cell model geometry for the bath flow simulation.

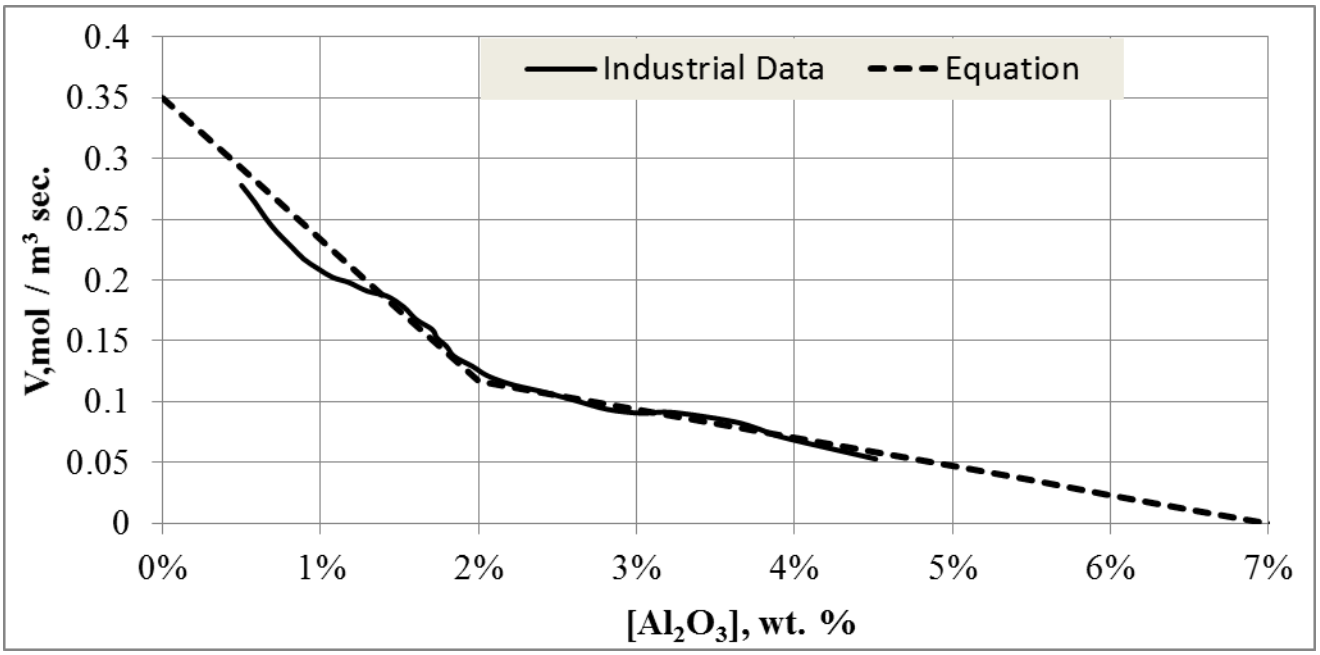

Figure 6: Dissolution rate of alumina in "industrial baths" at a temperature of 960 °C, from Frovlov *et al.* [14] and the model of Equation 26.

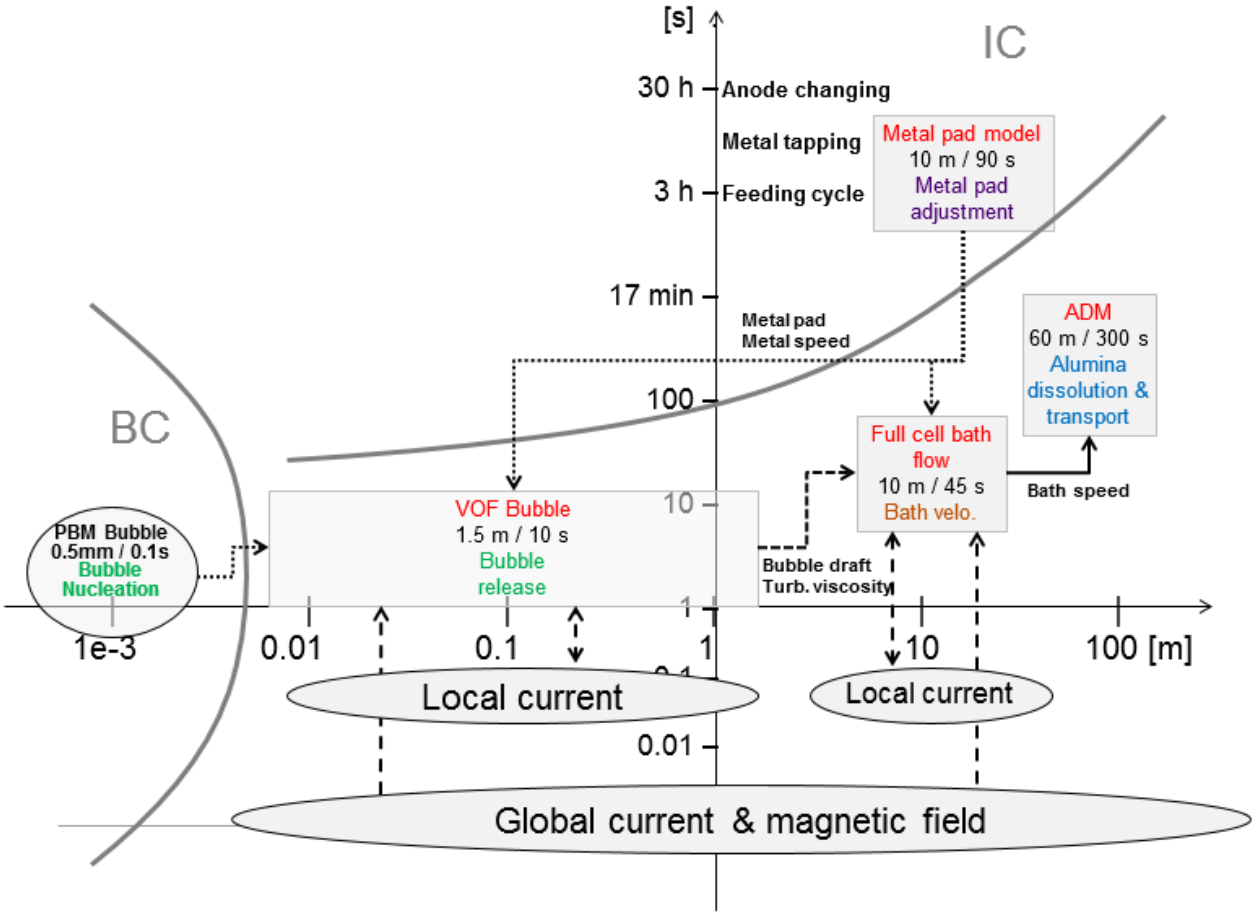

Figure 7: Location of main phenomena in length/time diagram.

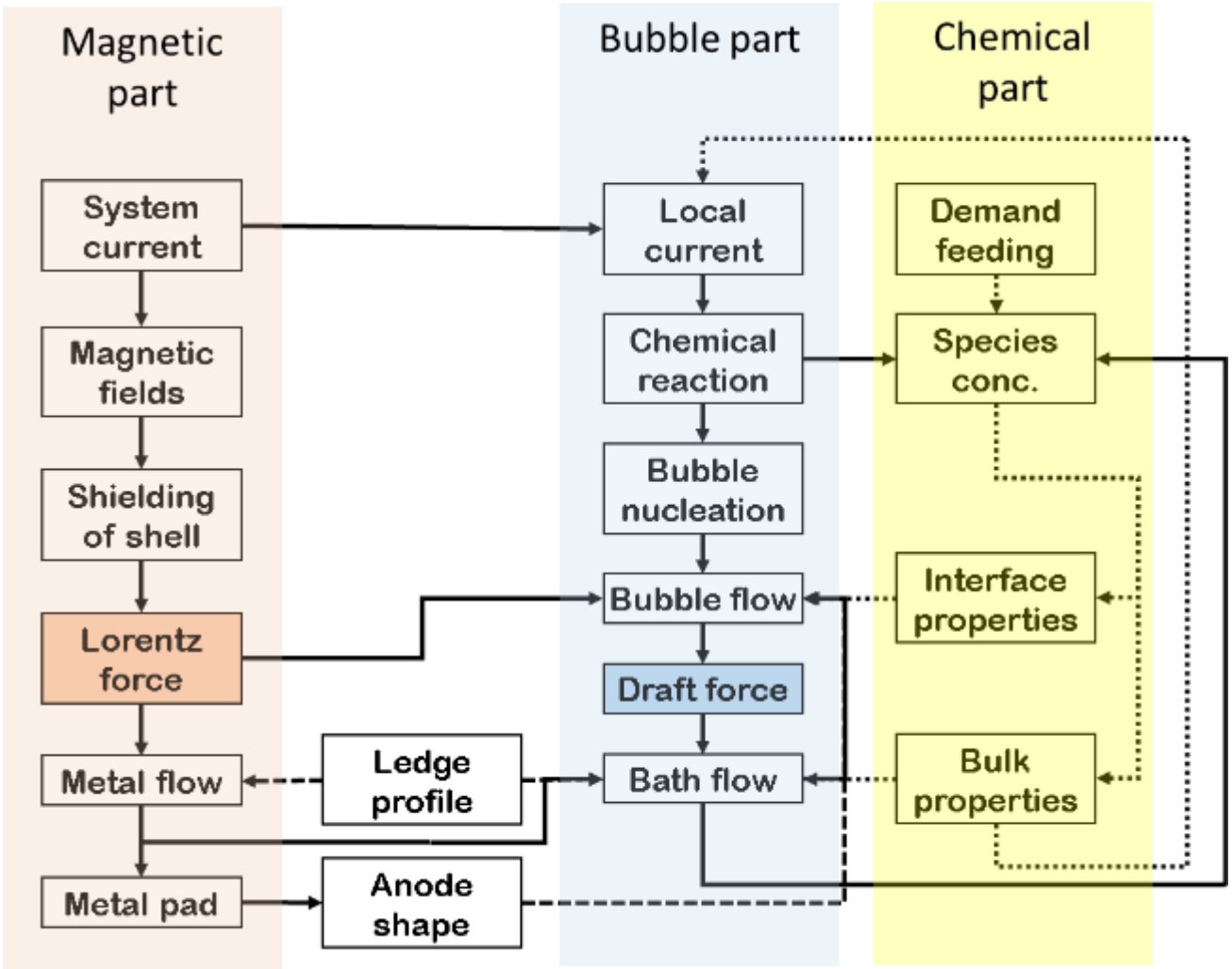

Figure 8: Primary coupling behaviour of the three process parts.

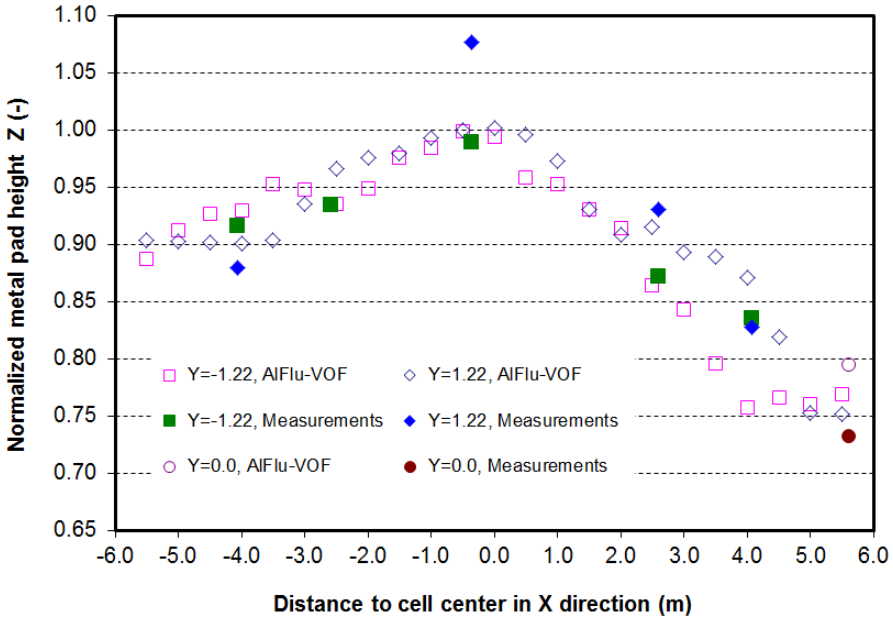

Figure 9: Comparison of metal pad height with simulation and measurements.

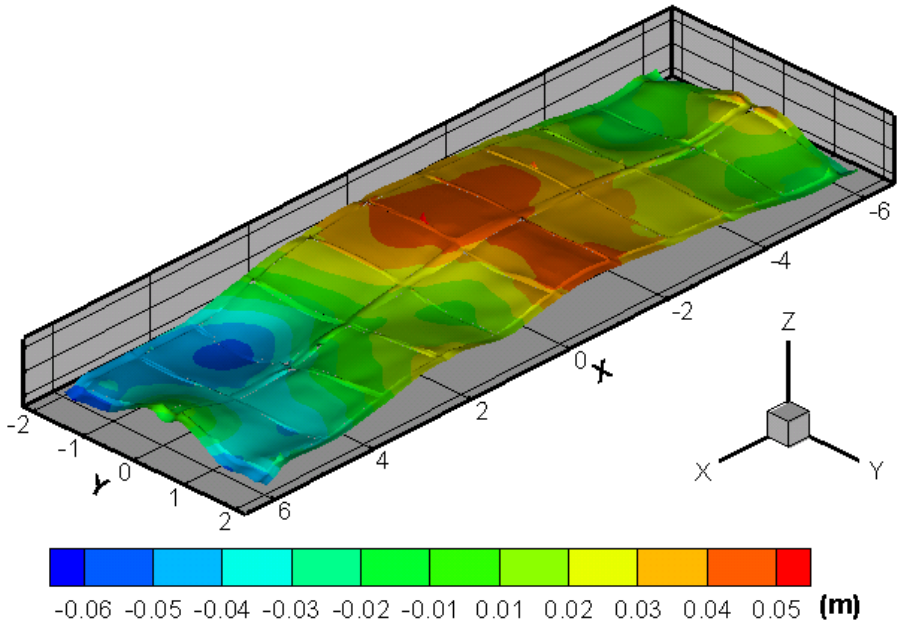

Figure 10: (a) The metal pad profile and deformation.

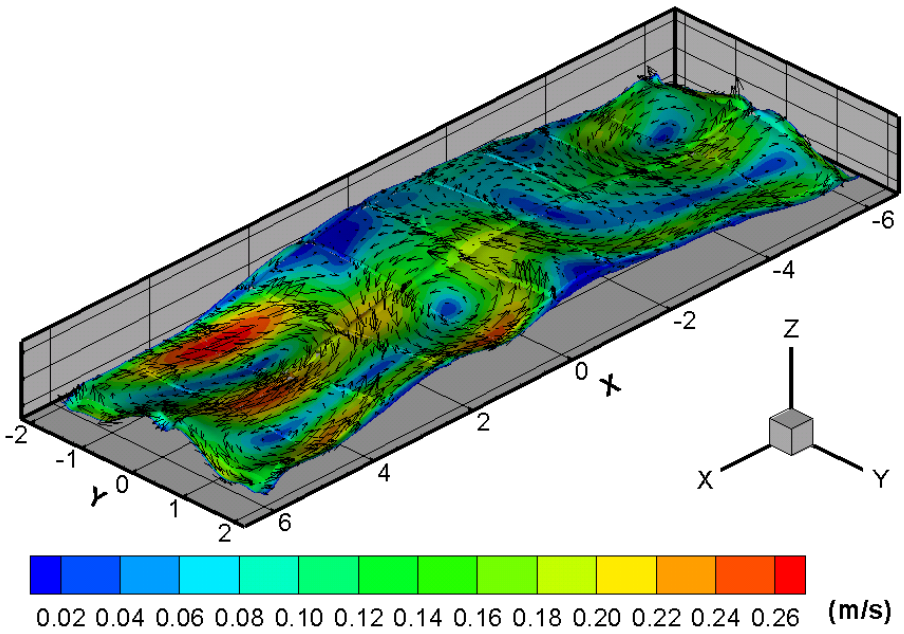

Figure 10: (b) the velocity distribution on the metal pad predicted by the simulation.

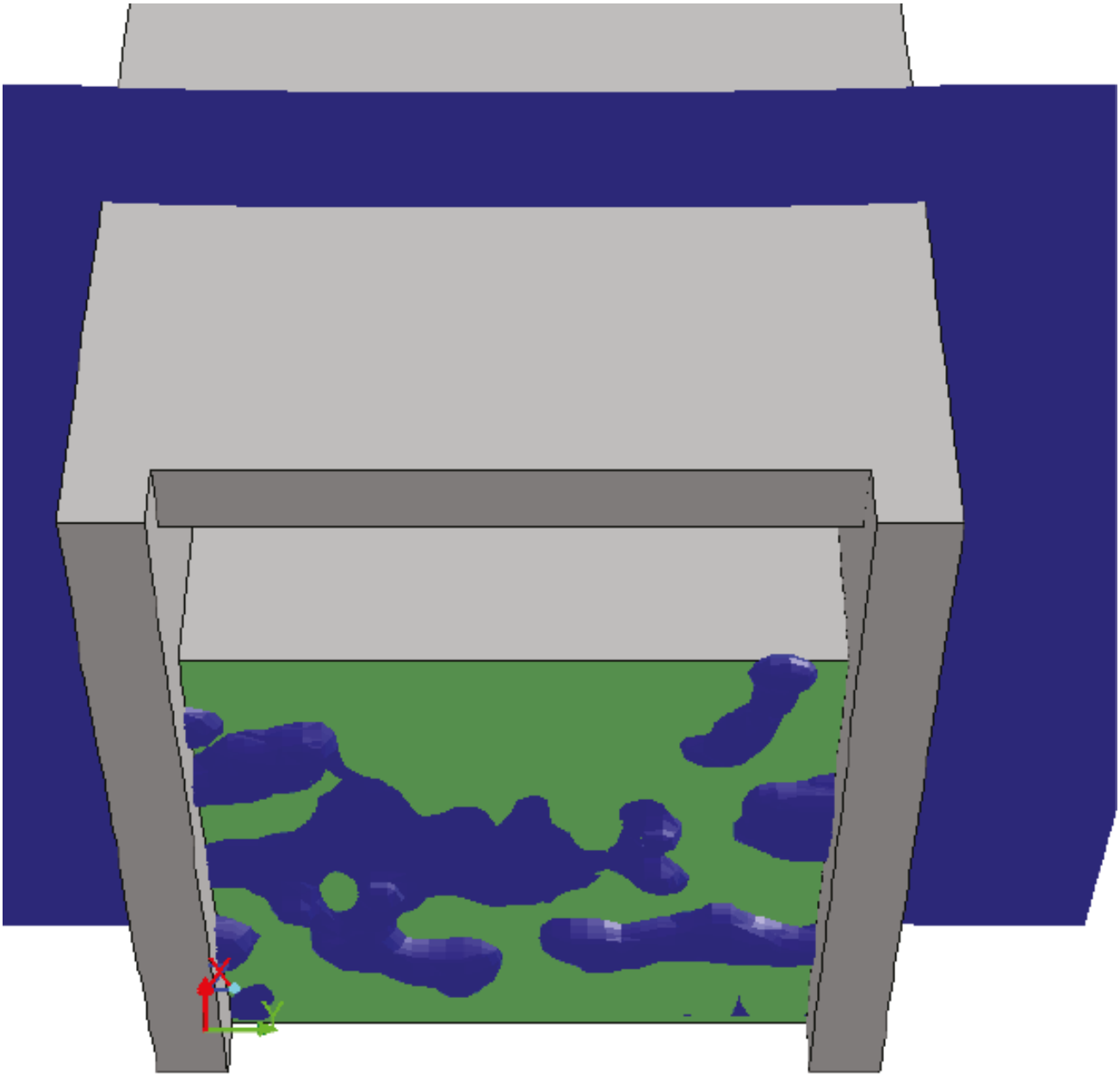

Figure 11: Typical view of simulated gas evolving anode. Gas is shown in blue, while the active anode surface is highlighted in green.

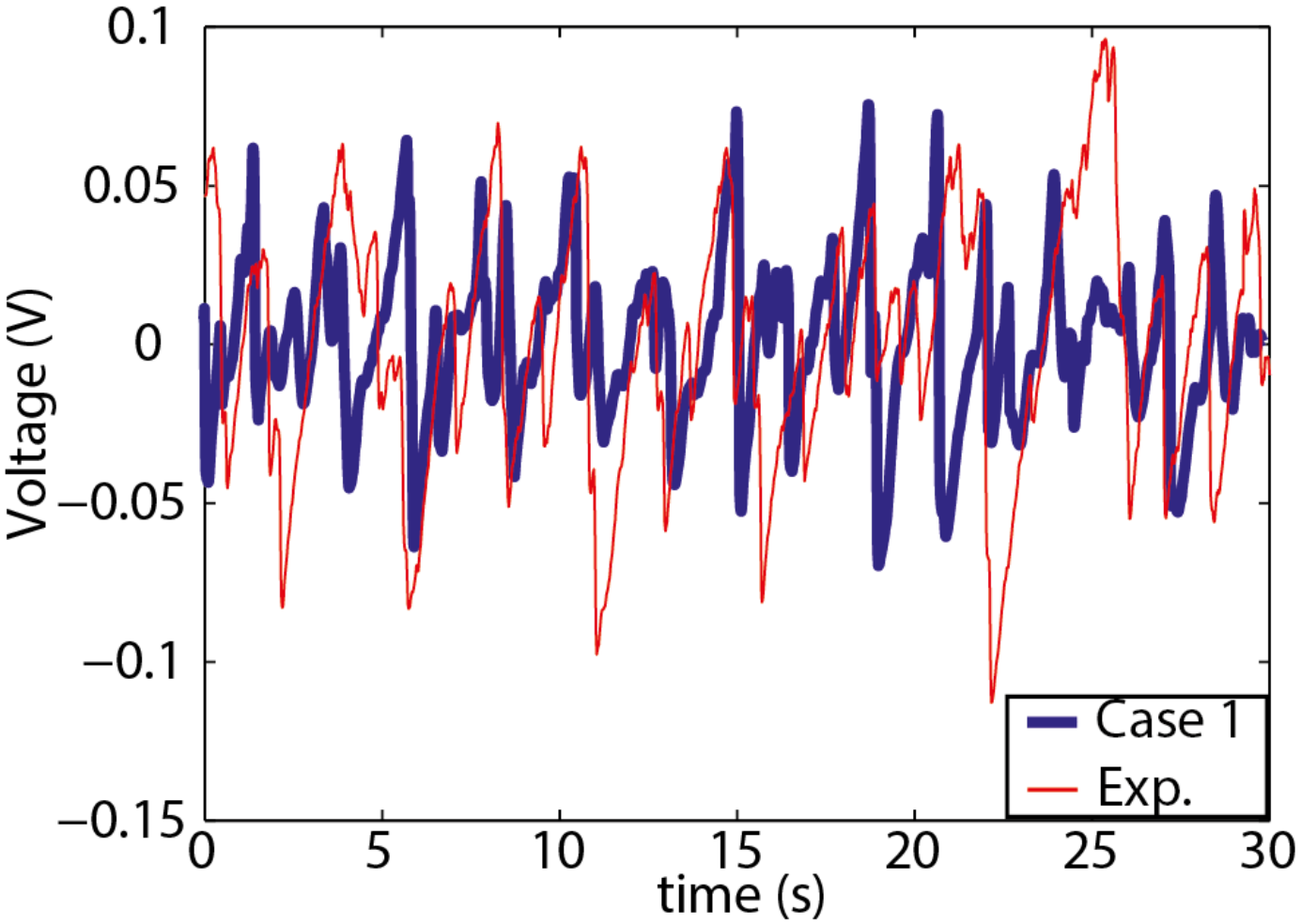

Figure 12: Simulated (blue) and experimental (red) voltage curves for current density 0.8 A m^{-2}, 4 cm ACD and 2^{o} anode inclination.

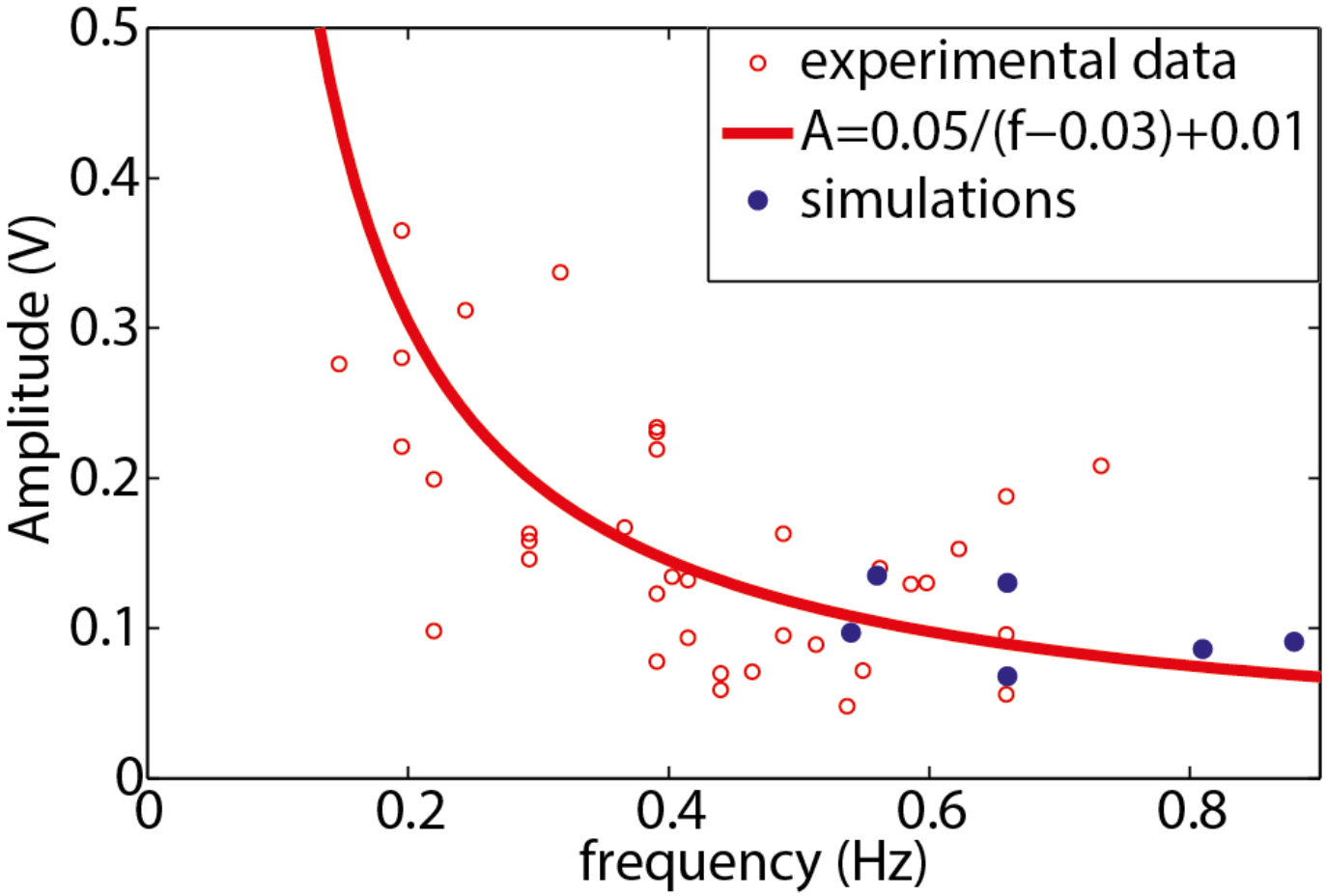

Figure 13: Summary of measured (open circles) and simulated (closed circles) voltage vs. frequency plot under various operating conditions, compared to a least squares fit of the form proposed by [33].

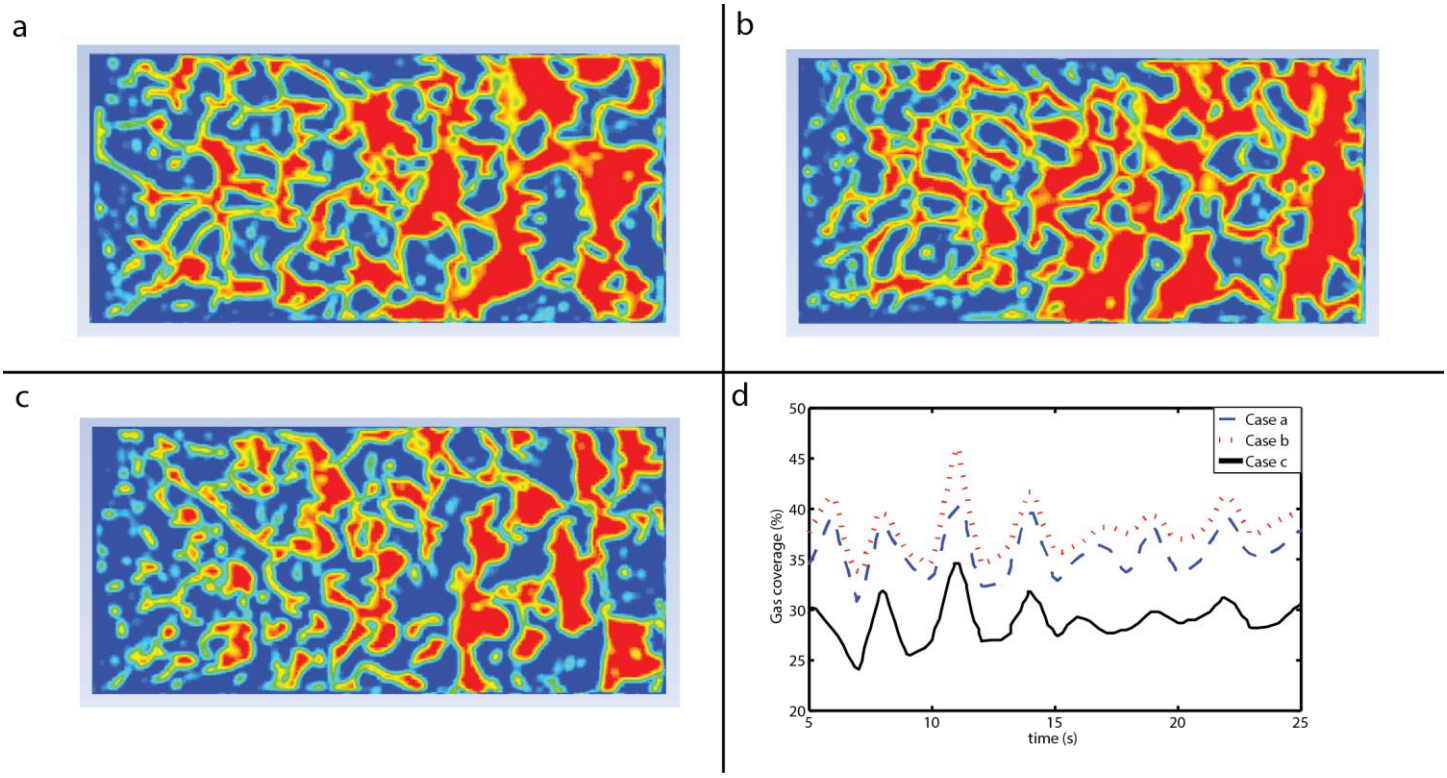

Figure 14: Gas accumulation (red) under the anode depending on titling angle θ (a and b, θ=2^{o}, c; θ=4^{o}) and current density, (a and c, J=8000 A/m^2, b; J=11000 A/m^2) and resulting gas coverage for each of the cases (d).

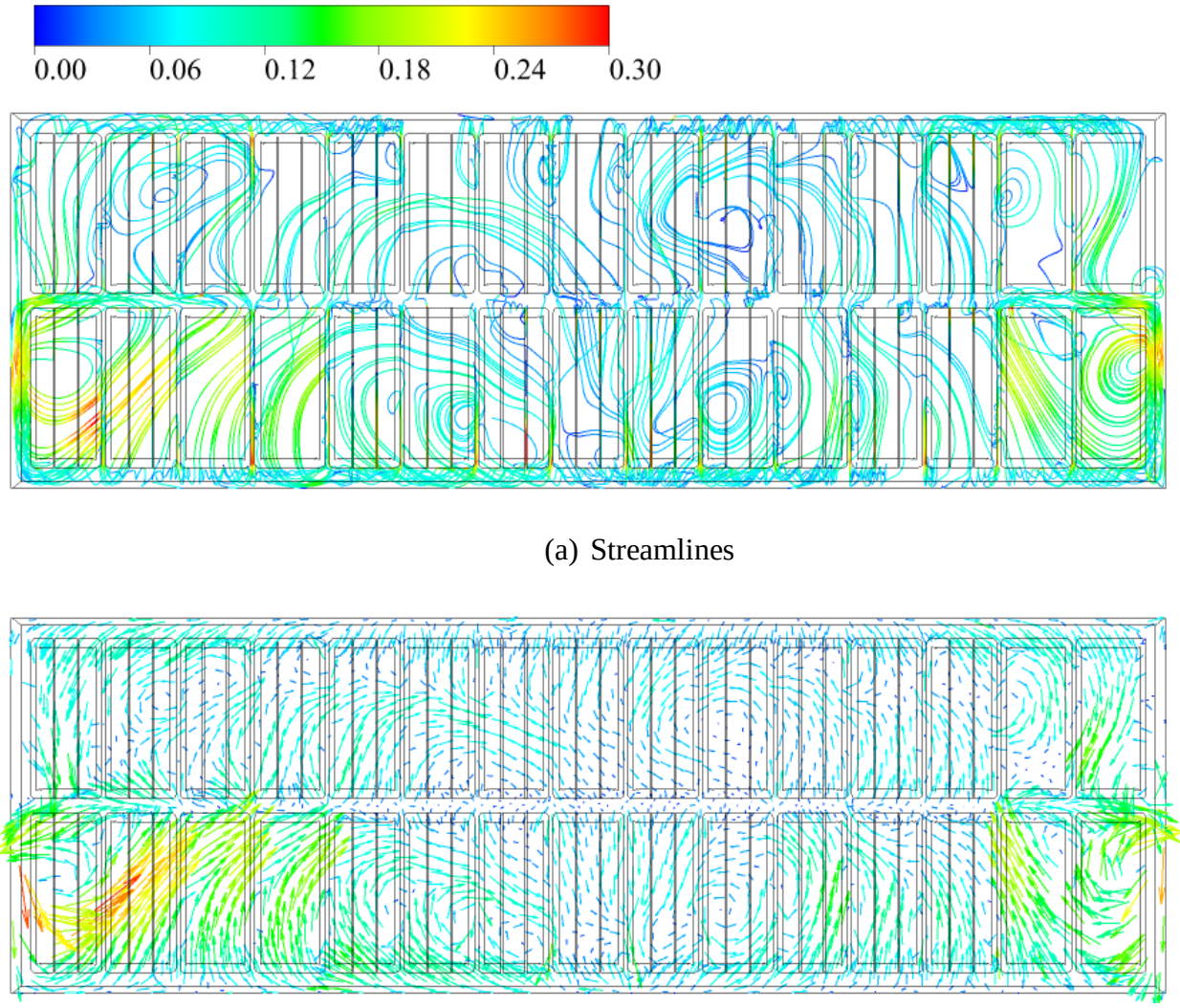

(a) Streamlines

(b) Velocity vectors on a plane through the ACD

Figure 15: Coupled bath flow field in the cell on a plane through the ACD (top view).

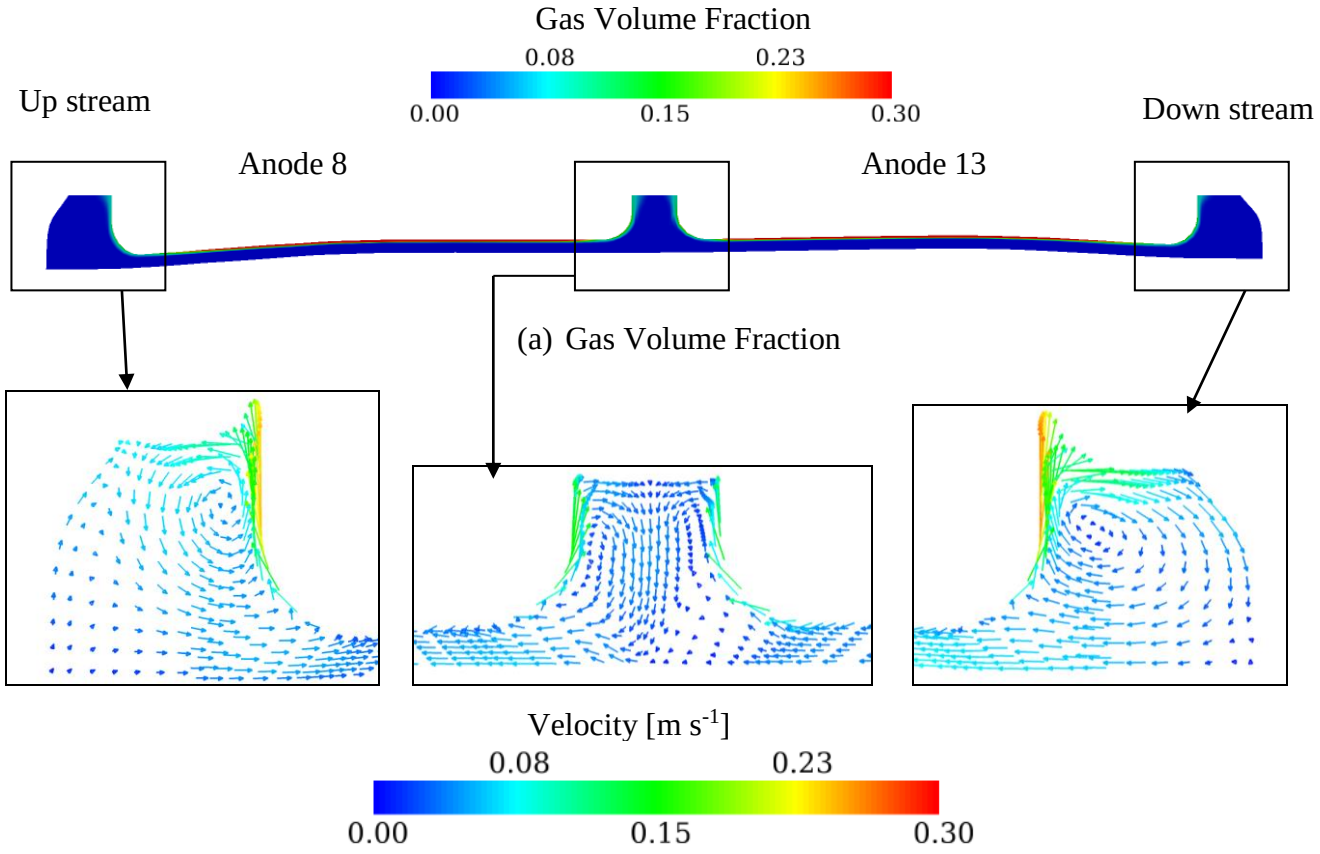

(b) Bath Velocity Vectors

Figure 16: Gas hold up on the vertical plane A-A (in Figure 5) with inserts showing detailed flow in the side and centre channels.

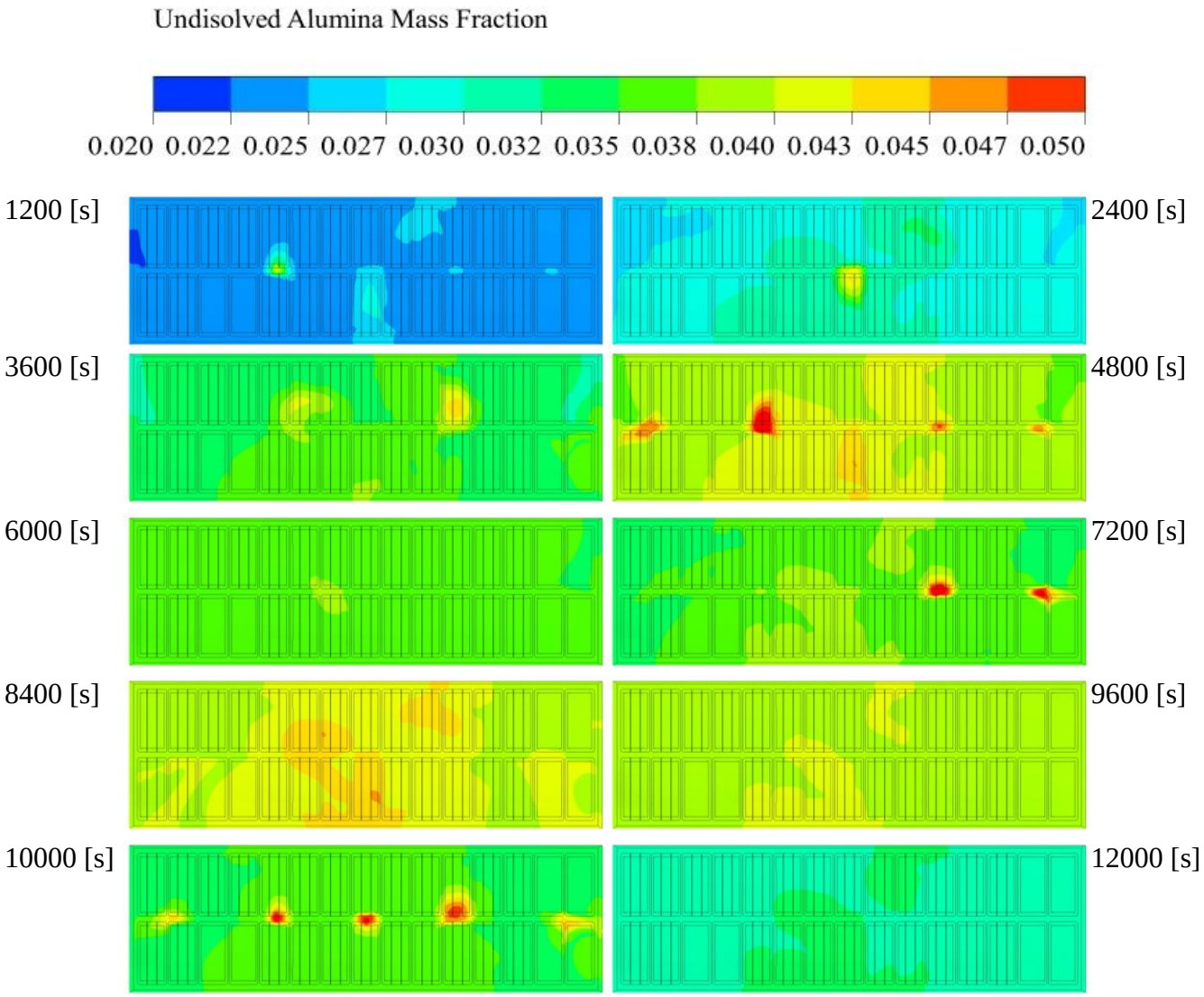

Figure 17: Undissolved alumina species during the first 12000 seconds of the feeding cycle.

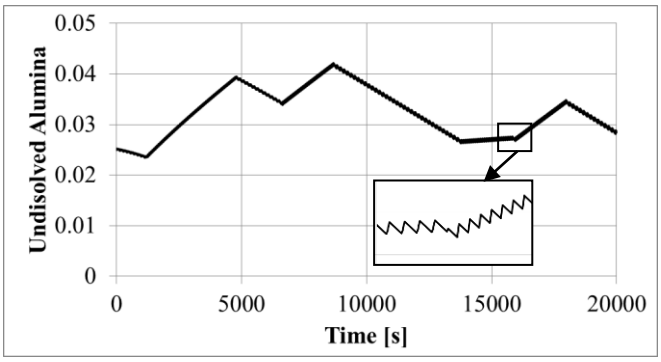

(a)

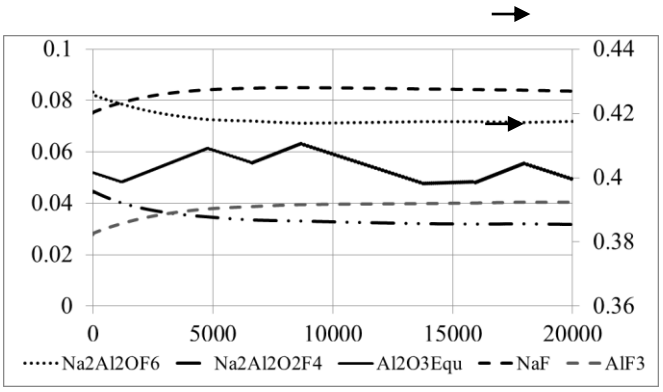

(b)

Figure 18: (a) Change in undissolved alumina mass fraction with time. (b) Change in species mass fraction with time, including calculated equivalent alumina mass fraction..